

A Conceptual Design for Deflection Device in VTDP System

Yongwei Gao (✉ gyw630@nwpu.edu.cn)

Northwestern Polytechnical University <https://orcid.org/0000-0001-7026-9273>

Jianming Zhang

Northwestern Polytechnical University

Long Wang

Northwestern Polytechnical University

Bingzhen Chen

Northwestern Polytechnical University

Binbin Wei

Northwestern Polytechnical University

Research

Keywords: vectored thrust ducted propeller, conceptual design, wind tunnel experiment, numerical simulation

Posted Date: August 27th, 2020

DOI: <https://doi.org/10.21203/rs.3.rs-64863/v1>

License:   This work is licensed under a Creative Commons Attribution 4.0 International License.

[Read Full License](#)

Version of Record: A version of this preprint was published at Advances in Aerodynamics on January 21st, 2021. See the published version at <https://doi.org/10.1186/s42774-020-00050-x>.

Abstract

A conceptual design for a deflection device of a Vectored Thrust Ducted Propeller (VTDP) system was proposed to achieve effective hovering control. The magnitude of the lateral force that was applied to maintain balance while hovering was examined. A comparison between the experimental and numerical results for the 16H-1 was made to verify the numerical simulation approach. The deflection devices of the X-49 and the proposed design were analyzed using numerical simulations. The results indicated that the proposed design provided a larger lateral force and lower power consumption.

1 Introduction

A traditional helicopter with a tail rotor is limited in its forward flight speed due to the compressibility effect of the advancing blades and flow separation of the retreating blades. The level-flight cruise speed for conventional helicopters is approximately 150 kts. To further enhance the cruise speed, vectored thrust ducted propeller (VTDP) technology was proposed[1–4]. The VTDP system is installed on the aft end of the fuselage and replaces the conventional tail rotor. The VTDP system usually includes a ducted propeller[5, 6], and flow deflection devices. The flow deflection devices can be vertical vanes or other mechanisms. In addition to providing anti-torque and yaw control, the VTDP can provide extra forward thrust and trim control[7, 8]. A compound helicopter with VTDP technology has a higher forward flight speed, better controllability and agility and larger payload capabilities.

The Piasecki 16H and Piasecki X-49 use VTDP systems[9]. The Piasecki 16H was a series of compound helicopters produced in the 1960s. The first version of the Pathfinder, the 16H-1 version, first flew in 1962. A similar but larger Pathfinder II, the 16H-1A, was completed in 1965. The Piasecki X-49 “SpeedHawk” is an American four-bladed, twin-engine, experimental, high-speed compound helicopter under development by Piasecki Aircraft.

Similar deflection devices for the 16H-1 and X-49A are displayed in Fig. 1 and Fig. 2, respectively. The 16H-1 uses vertical vanes as deflection devices, and the X-49A uses a swerving sector (similar to a semi-spherical shell) as a deflection device. During flight, the vanes do not undergo deflection or sector withdrawal. While hovering or yawing, the vanes undergo deflection or sector extension to provide the proper torque.

Hovering for VTDP systems poses more restrictions than forward flight in that hovering state should provide a larger lateral force and a smaller axial force. Different forms of the flow deflection devices are intended to have different effects.

In this paper, an alternative form of the flow deflection device is proposed. Based on numerical simulations, the proposed flow deflection device was proven to be superior to the VTDP systems of the 16H-1 and X-49. To verify the numerical results, experiments on the VTDP of the 16H-1 were carried out. After validating the simulation results, simulations were conducted on the VTDP of the X-49 and the conceptual VTDP proposed in the paper.

The paper is organized as follows. The experiments on the VTDP of the 16H-1 are first introduced, and then numerical simulations for this VTDP are presented. The experimental and simulation results are then compared. Subsequently, the numerical simulations for other VTDP systems are presented. Finally, a comparison is made to demonstrate the advantages of the new VTDP.

2 Computational Model Validation

2.1 Ducted Propeller Experiment

The performance of ducted propeller was tested in the NF-3 wind tunnel. An optical sensor was used to measure the rotor speed, and the voltage and current were also measured. The experimental model is shown in Fig. 3 and Fig. 4. The tip clearance ratio is defined as follows:

$$\delta = \frac{\Delta}{R} \quad (1)$$

where Δ is the blade tip clearance, R is the inner radius of the duct, and δ is the tip clearance ratio. The inner diameter of the duct was denoted as D , and tip clearance ratio δ was 0.91%.

2.2 Computational Model

Fig. 5 shows the computational model. An unstructured grid was used for the calculations. Multiple coordinate systems were established to simulate the relative motion between the propeller and duct. Accordingly, the computational domain was divided into two sub-domains: a rotating domain and a stationary domain[10]. The propeller was in the rotating domain, and the duct was in the stationary domain. The two domains were used to generate computational meshes, as shown in Fig. 5.

Considering the periodicity of the blade rotation and the symmetry of the duct, the stationary surfaces and rotating region were divided into four segments, and only one of them was used in the numerical calculations. The mesh was properly refined along the leading edge of the propeller, the lip of the duct, and the clearance of the tip, as shown in Fig. 6 and Fig. 7.

2.3 Comparison of Experiments and Simulations

As shown in Fig. 8 and Fig. 9, the experimental results were in good agreement with the calculated results.

3 Investigation Of 16h-1

3.1 Hovering Experiment of 16H-1

The experiment was performed on the ground. The experimental model was similar to the VTDP of the 16H-1. The side and rear views are displayed in Fig. 10 and Fig. 11, respectively. The detailed model

dimensions are listed in Table 1.

Table 1 Main parameters

Component	Parameter	Value
Duct	Inlet diameter	644 mm
	Outlet diameter	618 mm
	Length	232 mm
Propeller	Number of blades	6
	Diameter	593 mm
	Hub diameter	75 mm
	Airfoil	ARAD
	Installed angle of blade tip	10°
Horizontal vane	Chord	92 mm
	Span	602 mm
	Airfoil	NACA 0012
Vertical vane	Chord	185 mm
	Span	493 mm / 600 mm / 493 mm
	Airfoil	NACA 0012

The model was set on an experiment table, which contained a six-component balance system connected to the model. An electric motor was connected to the propeller by a transmission shaft. The propeller was driven by the electric motor with a power rating of 100 kW. Because the hovering state was of interest, there was no free stream. While testing, the rotation speeds of the propeller and deflection angles of the vanes were under control. The axial and lateral forces were measured by a balance system. The power of the VTDP was calculated using the electrical current and voltage measurements, and the calibration was carried out before the experiment. The purpose of the experiments was to provide data to compare with the numerical simulations to verify their reliability. After the simulations were complete, a comparison with the experiments was performed.

3.2 Numerical Simulation of 16H-1

The numerical simulation was performed using ANSYS CFX. The Reynolds-averaged Navier–Stokes (RANS) equations were solved. The general connection interface model was Frozen-Rotor. The advection schemes were high resolution, and the turbulence scheme was a first-order upwind scheme. The turbulence model was the shear-stress transport (SST), and the dimensionless wall spacing $y^+ < 1$ for all the walls.

3.3 Comparison Between Experiment and Numerical Simulation for 16H-1

For both the experiments and numerical simulations, the deflection angle ϕ of the vertical vanes was fixed at 20°, and the deflection angle of the horizontal vanes was kept at 0°. The rotation speed of the propeller was adjusted. The comparisons of the axial force, lateral force, and power of the 16H-1 from the experiments and the numerical simulation are shown below.

Fig. 13 displays the comparison of the axial force for different rotation speeds. The results from the first and second experiments, which are, respectively, labeled as “Experiment 1” and “Experiment 2” in the

legend, were similar. The calculated axial force was underestimated by less than 10%. However, the trend was similar to

that of the experiment.

Fig. 14 shows the comparison of the lateral forces for different rotation speeds. The lateral force was slightly overestimated. Nevertheless, the overall trend was the same.

Fig. 15 shows a comparison of the power for different rotation speeds. The power curves for the two experiments and numerical calculations coincided.

These comparisons demonstrated that the numerical simulation has the potential to be used to estimate the VTDP, at least for the axial force, lateral force, and input power. Based on the comparison, the proposed simulation method can be used to further explore the different VTDP configurations.

3.4 Further Numerical Results for 16H-1

In the simulations discussed in the previous section, the deflection angle of the vertical vanes was fixed. In the simulations discussed in this section, the rotation speed was fixed at $n = 6500$ rpm, and the deflection angles were varied.

Fig. 16 displays the axial force or thrust at different deflection angles. The hollow markers represent the total axial force for the VTDP of the 16H-1, and the solid markers represent the axial force components from the propeller, duct, and vertical vanes. With an increase in the deflection angle, the thrust of the propeller increased, the drag of vertical vanes increased, and the thrust of duct increased. As a result, the whole thrust of the VTDP system decreased monotonically.

Fig. 17 shows the lateral force at different deflection angles. The total lateral forces of the system and the vanes increased first and then decreased. The maximum forces occurred near $\phi = 40^\circ$. The lateral force of the duct decreased with the increase in ϕ .

Fig. 18 shows the power variations at different deflection angles. The maximum consumed power occurred at the same deflection angle as that of the maximum lateral force in Fig. 17.

4 Numerical Simulation For X-49

The numerical simulation results for the X-49 were similar to those for the 16H-1. As shown in Fig. 19, the outer deflector completely opened, and the deflection angles of the vertical vane were 50° and 60° . The numerical results are shown in Table 2.

Table 2 Numerical results for X-49

Deflection angle of vanes	Axial force/N	Lateral force/N	Power/kW
50°	263	306	19.54
60°	208	304	19.40

5 Conceptual Design For The Deflection System Of Vtdp

The conceptual design for deflection system is displayed in Fig. 20. In the conceptual design, the duct was prolonged, eliminating the horizontal and vertical vanes of the 16H-1. Two rotatable slices that were parts of the prolonged duct replaced the extra outer deflector in the X-49. As displayed in Fig. 21, the first slice rotated in an anticlockwise direction, and the second slice rotated in a clockwise direction. While operating, the two slices constituted a nozzle that was similar to a vectored thrust nozzle.

Fig. 22 shows the grid at the horizontal central section. Fig. 23, Fig. 24 and Fig. 25 show the variations of the axial force, lateral force, and power with the deflection angle ψ .

6 Comparison Between 16h-1, X-46 ,and Conceptual Design

6.1 Force and Power Consumption

The lateral forces between the three deflection systems are compared in Fig. 26. The maximum lateral forces for the 16H-1 and X-49 occurred at $\phi = 40^\circ$ and $\phi = 50^\circ$, and the lateral forces for the proposed design at different deflection angles are compared in Fig. 26. The maximum lateral force for the 16H-1 was smaller than those of the other two deflection systems. The lateral forces of the proposed design for deflection angles from 90° to 120° were comparable with the maximum force of the X-49, although the maximum lateral force of the proposed design at $\psi = 110^\circ$ was a bit larger than that of the X-49.

For hovering, a larger lateral force and smaller axial force are preferable. Therefore, Fig. 27 compares the axial forces. The axial force for the proposed design at $\psi = 110^\circ$ was smaller than that of the 16H-1 at $\phi = 40^\circ$ and X-49 at $\phi = 40^\circ$, where these angles corresponded to the maximum lateral forces. The Fig. 27 indicated that in a range of deflection angles for the proposed design, the axial force was always smaller than those of the other two systems.

Fig. 28 compares the power. The consumed power for the proposed design was the smallest. These comparisons demonstrated that the proposed design provided a high lateral force with smaller values of the axial force and consumed power.

6.2 Streamlines and Pressure Contours

The streamlines and pressure contours are displayed in Fig. 29, Fig. 30 and Fig. 31, providing further information for the proposed design. According to the principle of momentum conservation, the forces exerted on the VTDP, including the axial and lateral forces, are determined by the pressure on the VTDP,

the airflow deflection, and the mass flux, which can be explained by Fig. 32. The axial velocity and pressure of the free stream were V_0 and P_0 . The velocity increased and the pressure decreased as the airflow approached the propeller. The pressure before the propeller was P' . After the flow passed through the propeller, the pressure increased to $P' + \Delta P$, and the axial velocity increased to V_1 . The area of the propeller disk was A_1 , and the area of the outlet was A_2 . At the outlet, the velocity further increased, and the pressure decreased to P_0 . The flow from the outlet of the duct was assumed to be deflected completely. The average deflection angle of the flow was Φ , and the velocity was V_2 . According to the principle of momentum conservation, the overall axial force of the VTDP system was

$$T = \dot{m}(V_2 \cos \Phi - V_0) = \rho A_1 V_1 (V_2 \cos \Phi - V_0) \quad (2)$$

and the overall lateral force was

$$Z = \dot{m} V_2 \sin \Phi = A_1 V_1 V_2 \sin \Phi \quad (3)$$

Based on Eq. 2 and 3, the lateral force of the VTDP was related closely to the mass flux through the duct and the deflection angle of the flow. To increase the lateral force of the VTDP, the mass flux through the duct and/or the deflection angle of the flow should be increased. However, the two variables are coupled, and increasing the deflection angle of the flow would increase the blockage effect, which would lead to a reduction in the mass flux. To obtain the maximum lateral force of the VTDP system, the designer should balance the two variables.

For the VTDP, it is assumed that the deflection angle of the vanes and the deflection angle of the airflow were consistent. From the continuity equation, we obtain the following:

$$A_1 V_1 = A_2 V_2 \cos \Phi \quad (4)$$

For hovering, the incoming airflow velocity is zero. The thrust of the VTDP is

$$T = \dot{m} V_2 \cos \Phi = \rho A_2 (V_2 \cos \Phi)^2 \quad (5)$$

and the lateral force is

$$Z = \dot{m} V_2 \sin \Phi = 0.5 \rho A_2 V_2^2 \sin 2\Phi \quad (6)$$

7 Conclusion

A deflection device for a VTDP system was designed conceptually in this study. Part of the inspiration for the present design was drawn from careful examination of the flow in the VTDP using the principle of momentum conservation, and another was from a comparison of two existing deflection devices: the 16H-1 and X-49. The proposed design aimed to achieve effective hovering control, and therefore, the lateral force was most important. Moreover, the power for the VTDP was taken into consideration. To

verify the effectiveness of the proposed design, comparisons between the experiments and numerical simulations were made for the 16H-1. Similar numerical simulations for the X-49 and the proposed design were carried out. The numerical results indicated that the present design provided a larger lateral force with a lower power consumption

Abbreviations

VTDP: vectored thrust ducted propeller

SST: shear-stress transport

Declarations

Acknowledgements

We would like to thank to all the experimental staff of the NF-3 Wind Tunnel for their hand work.

Authors' contributions

All authors have participated equally during the manuscript preparation. The authors have read and approved the final manuscript.

Funding

No funding.

Availability of data and materials

The files supporting the result of this article are available upon request.

Competing interests

The authors have no competing interests.

Nomenclature

R inner radius of the duct, mm

Δ tip clearance ratio, -

C_p pressure coefficient, -

C_x force coefficient in the x direction, -

C_y force coefficient in the y direction, -

n	rotate speed, rpm
ψ	deflection angle for conceptual design, °
ϕ	deflection angle for 16H-1 and X-49, °
Z	lateral force, N
T	axial force, N
W	power, kW

References

1. Huanjin, Wang,Zheng Gao,Research on the Scheme of a High-Speed Helicopter [J]. Flight Dynamics, 200, 36(2): 38–42. DOI: 10.3969/j.issn.1002-0853.2005.01.010
2. Prasetyo Edi N, Yusoff AA, Yazid, Catur Setyawan K, Nurkas W, Suyono WA New Design Approach of Compound Helicopter[J]. WSEAS TRANSACTIONS on APPLIED and THEORETICAL MECHANICS. 2008, 3(9): 799–808
3. Kai Liu,Fuchen Ye
ADVANCES IN AERONAUTICAL SCIENCE AND ENGINEERING
Review and Analysis of Recent Developments for VTOL Vehicles [J]
10.16615/j.cnki.1674-8190.2015.02.004
Kai Liu,Fuchen Ye. Review and Analysis of Recent Developments for VTOL Vehicles [J]. ADVANCES IN AERONAUTICAL SCIENCE AND ENGINEERING. 2015, 6(2): 127–138,159.DOI: 10.16615/j.cnki.1674-8190.2015.02.004
4. Yu, Qiu (2008) X-49a "Speed Hawk" Verification Machine [J]. Weapon Equipment 1:46–47
5. ROTORS FOR IMPROVED MICRO AIR VEHICLE DESIGN
Jason L, Pereira. HOVER AND WIND-TUNNEL TESTING OF SHROUDED ROTORS FOR IMPROVED MICRO AIR VEHICLE DESIGN, Professor Inderjit Chopra Department of Aerospace Engineering, 2008
6. Jia xu, Ningjun Fan (2008) Research Status and Structural Design of Ducted UAV [J]. AERODUNAMIC MISSILE JOURNAL 1:10–12. DOI:10.16338/j.issn.1009-1319.2008.01.002
7. J.A.Yetter. Why do airlines want and use thrust reversers? A compilation of airline industry responses to a survey regarding the use of thrust reversers on commercial transport airplanes. NASA Technical Memorandum 109158. 1995
8. Qi Rao M, Sheng, Taofeng H, Zhidong Hu (2014) Yali Chen. Research on Engine Thrust Reverser. SCIENCE MOSAIC 2:91–94. DOI:10.13838/j.cnki.kjgc.2014.02.015
9. Prasetyo Edi N, Yusoff AA, Yazid, Catur Setyawan K, Nurkas W, Suyono WA New Design Approach of Compound Helicopter[J]. WSEAS TRANSACTIONS on APPLIED and THEORETICAL MECHANICS. 2008, 3(9): 799–808

10. Zhao, Zhu, Investigation on Rotor/Stator Interface Processing Method and Ansys is on Configuration and Aerodynamic of Tubine[D]. Master thesis, Nanjing: Nanjing University of Aeronautics and Astronautics, 2008

Figures

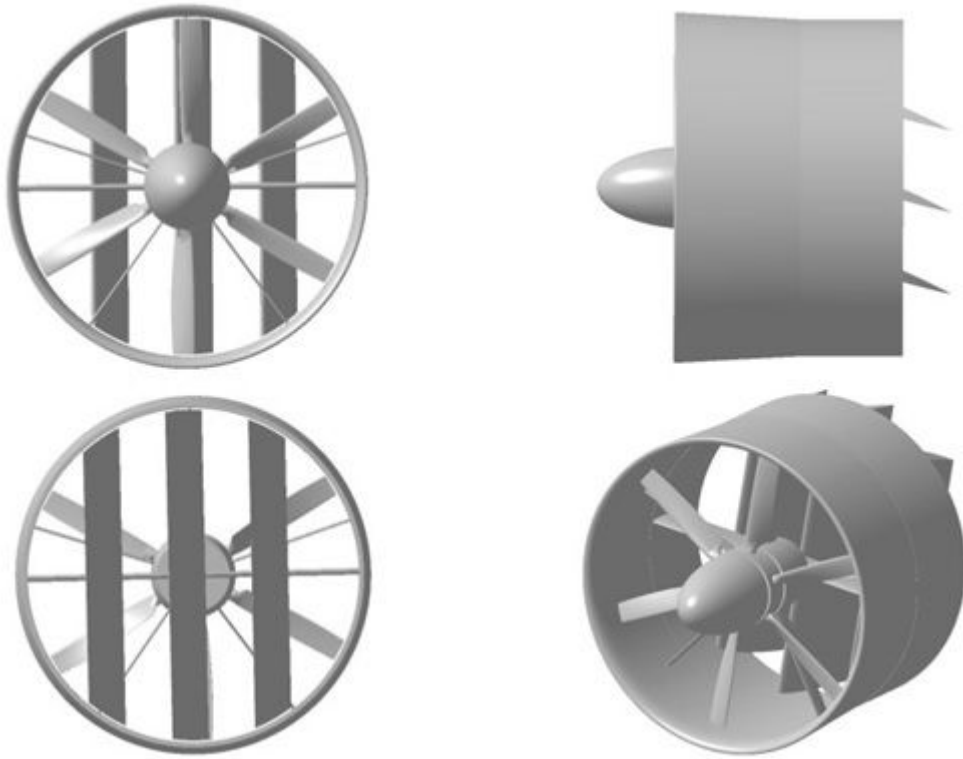


Figure 1

VTDP system for 16H-1

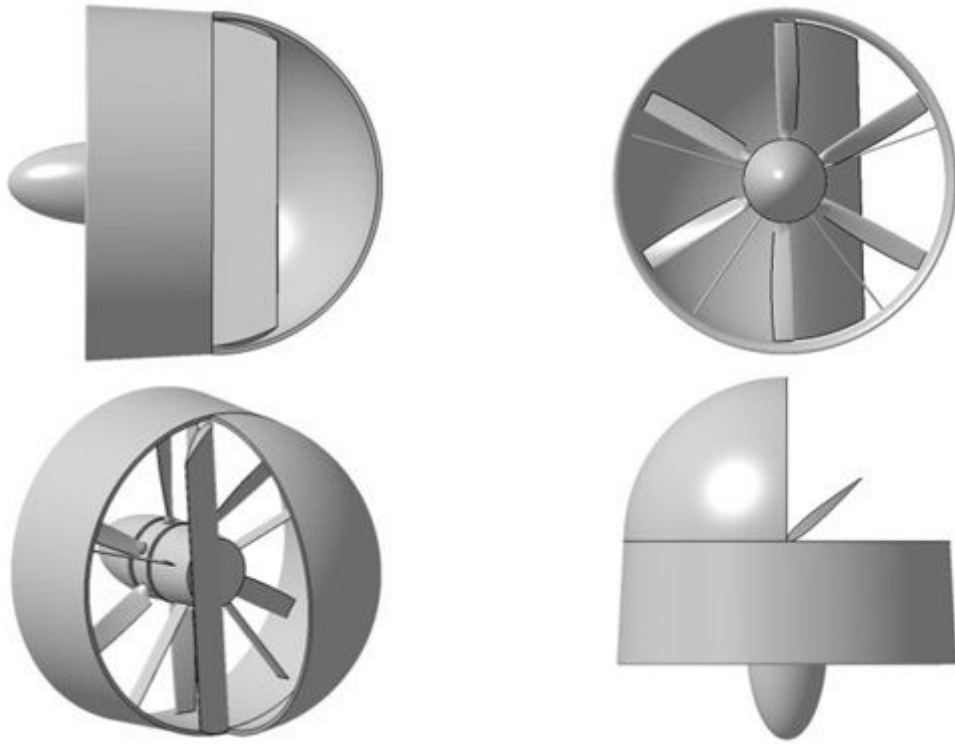


Figure 2

VTDP system for X-49A

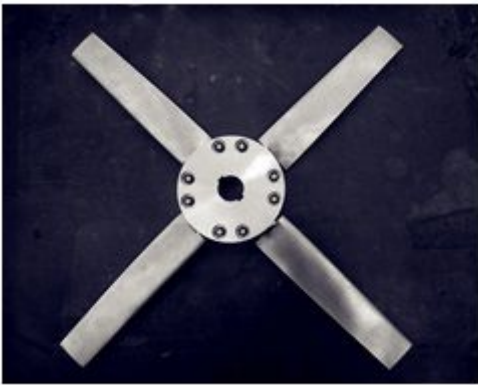


Figure 3

Propeller model



Figure 4

Model of ducted fan experiment

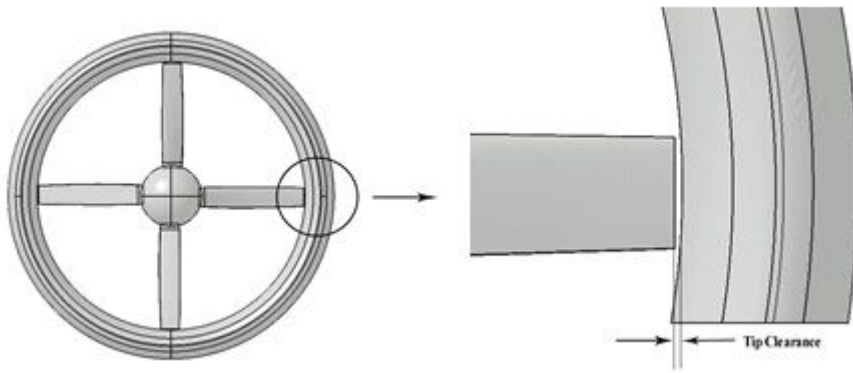


Figure 5

Computational model

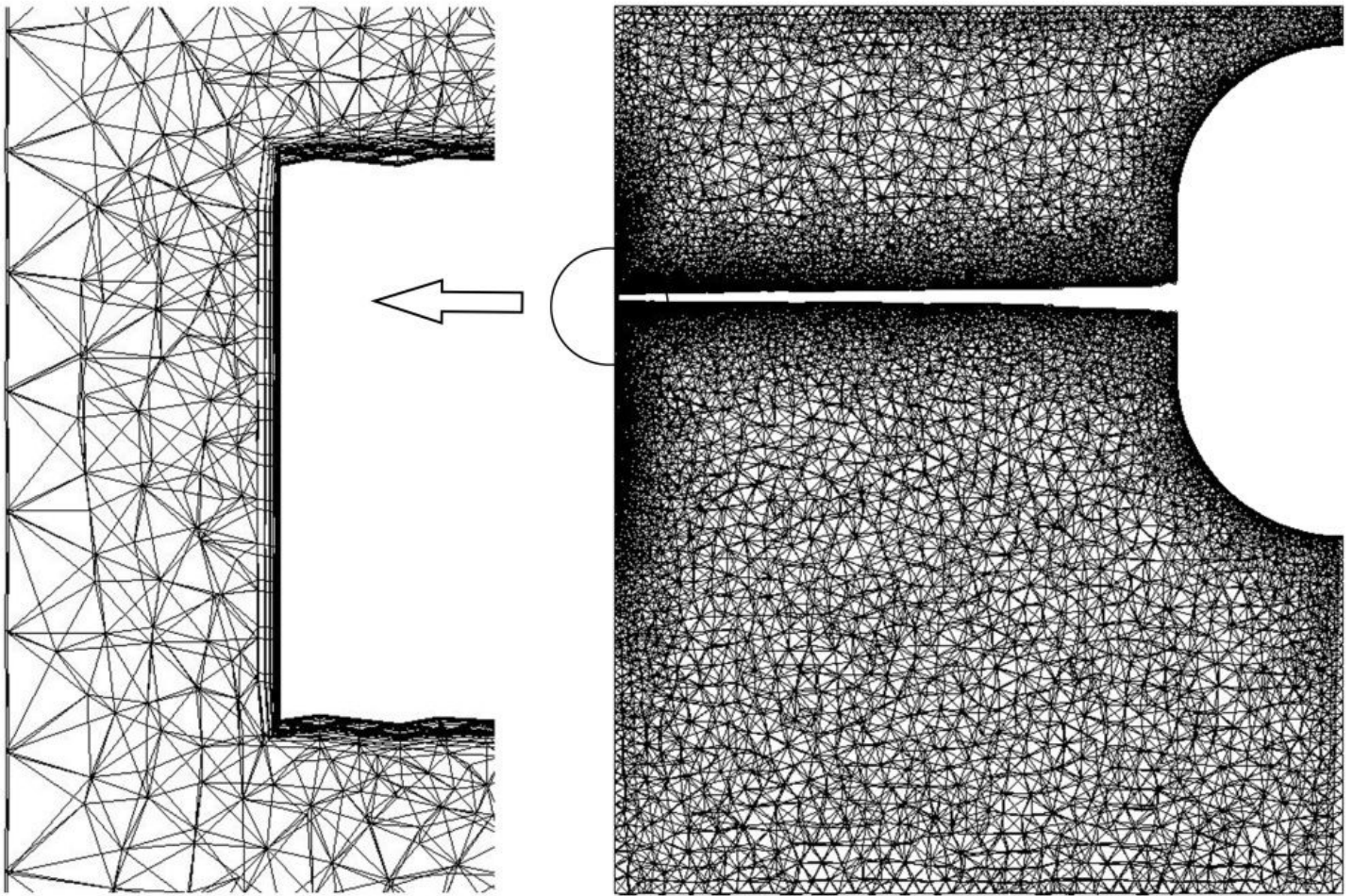


Figure 6

Mesh in the rotating domain

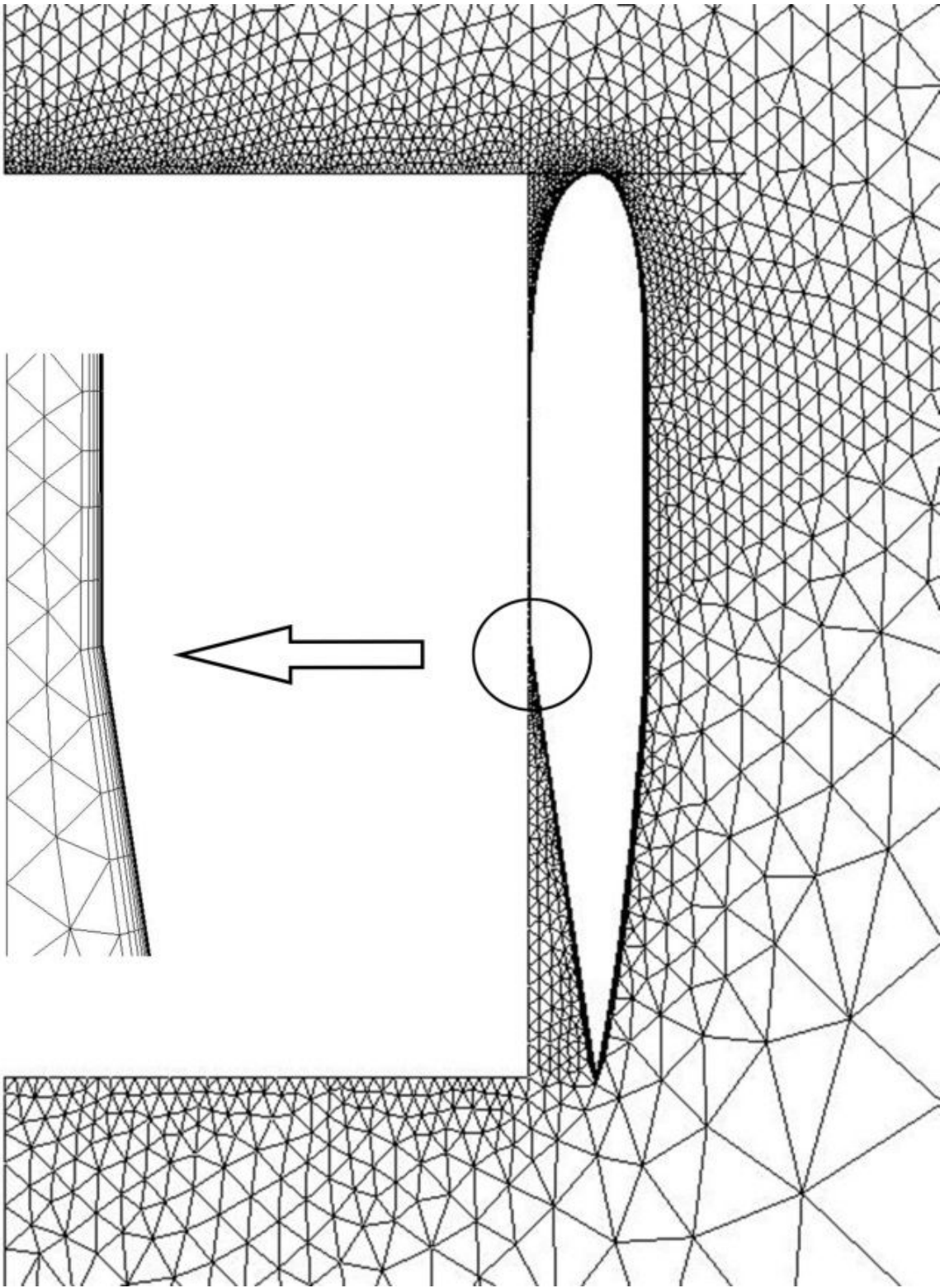


Figure 7

Mesh in the static domain

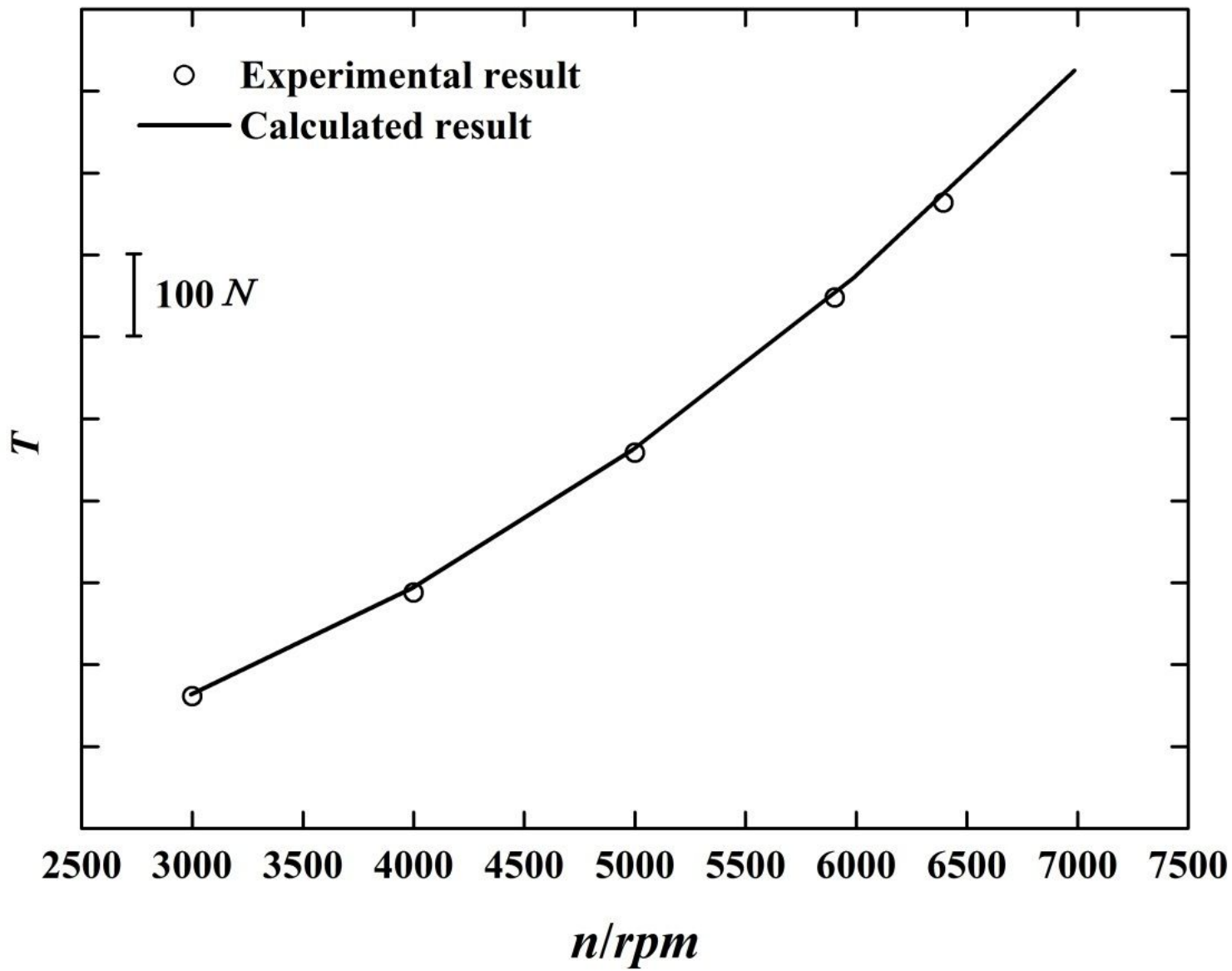


Figure 8

Thrust comparison

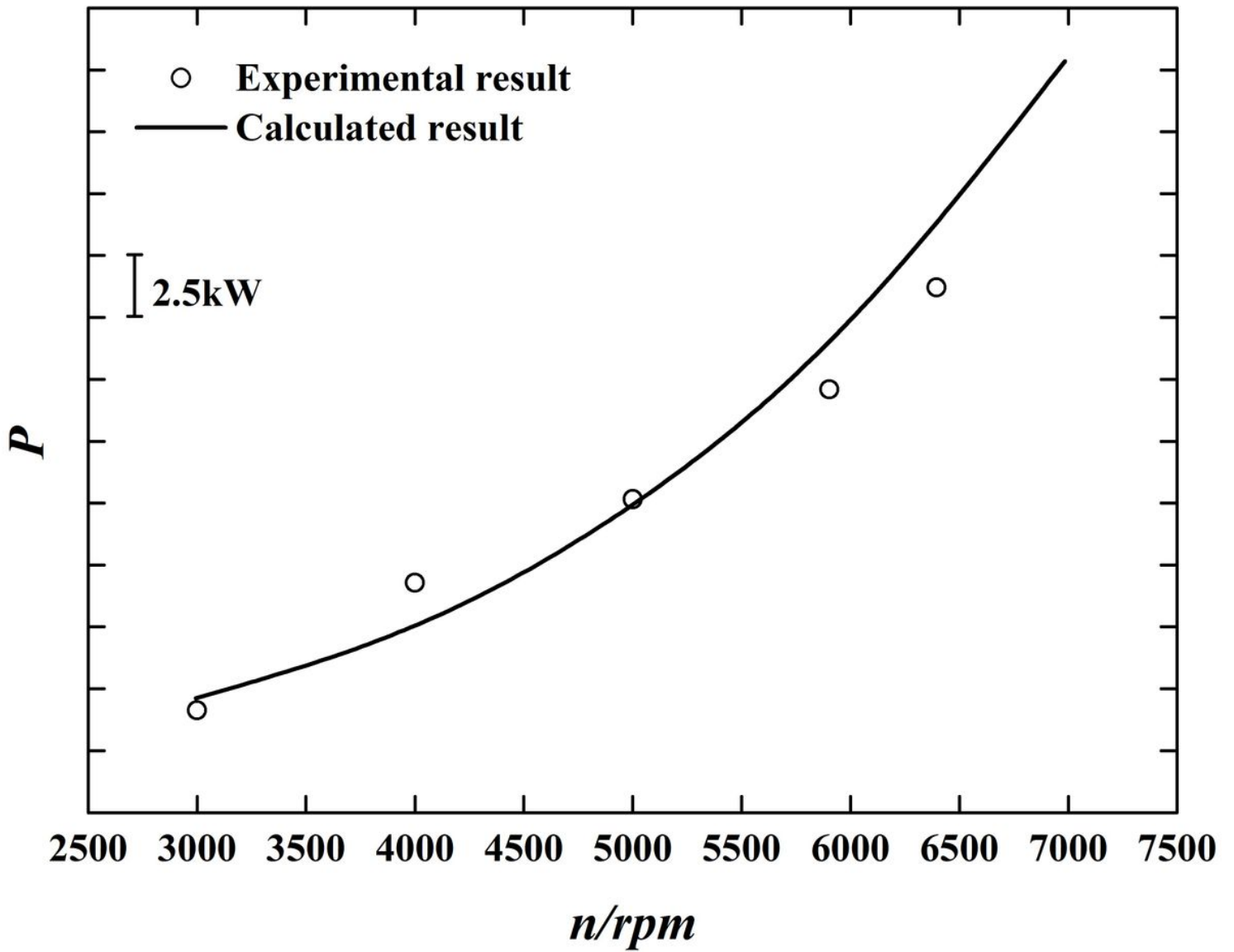


Figure 9

Power comparison

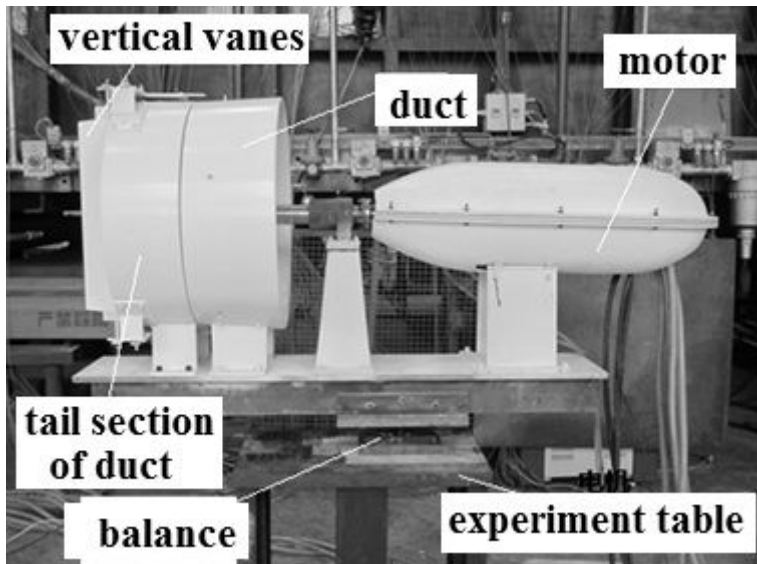


Figure 10

Side view

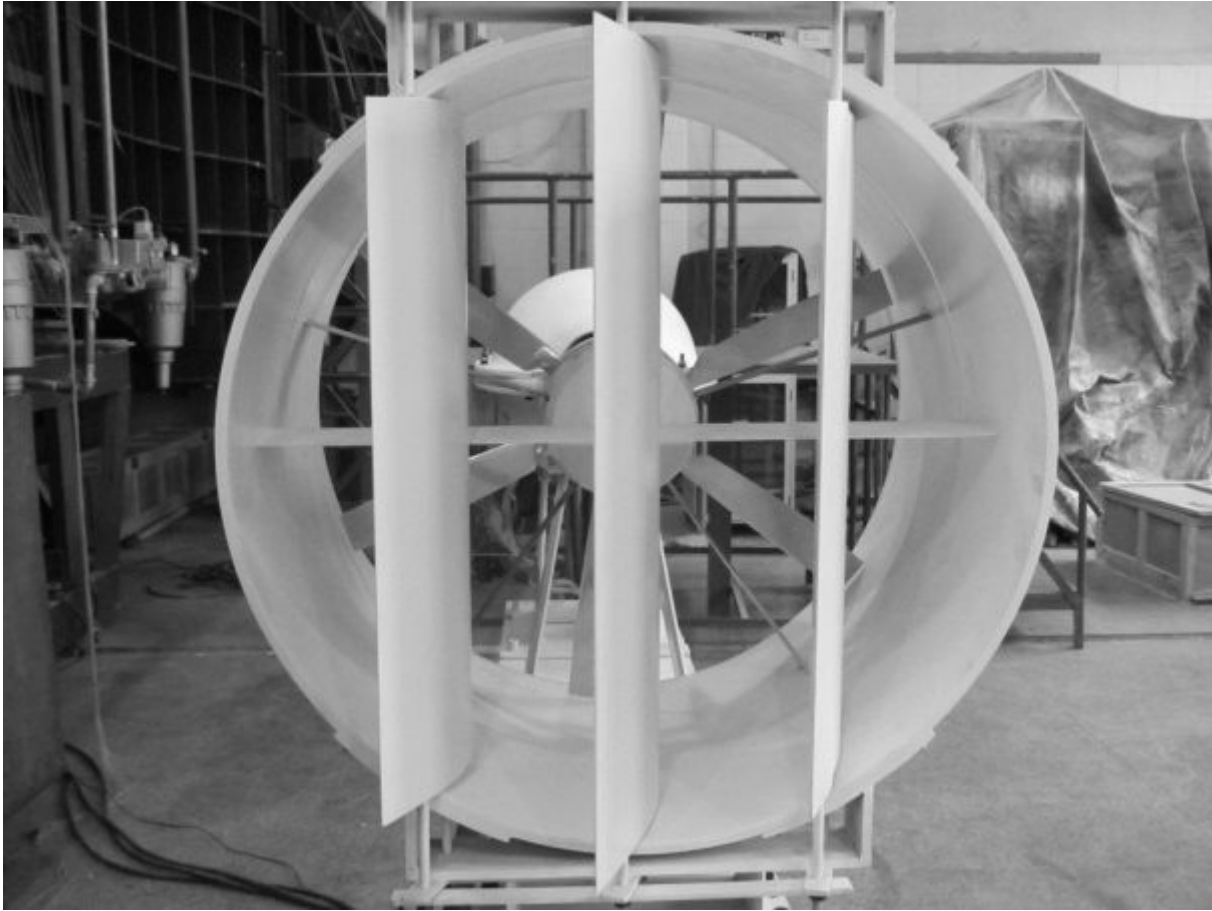


Figure 11

Rear view

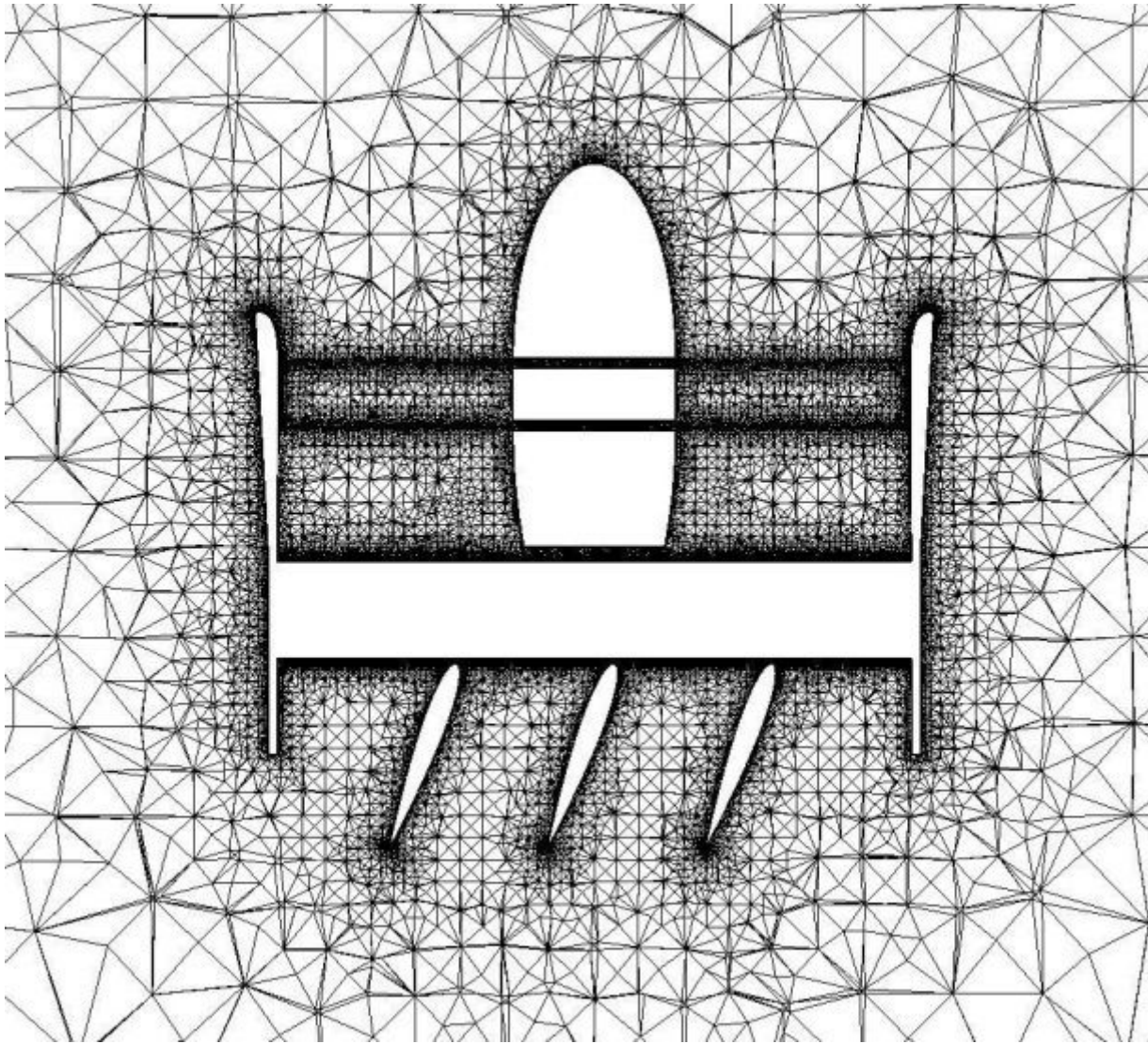


Figure 12

Horizontal central section meshes

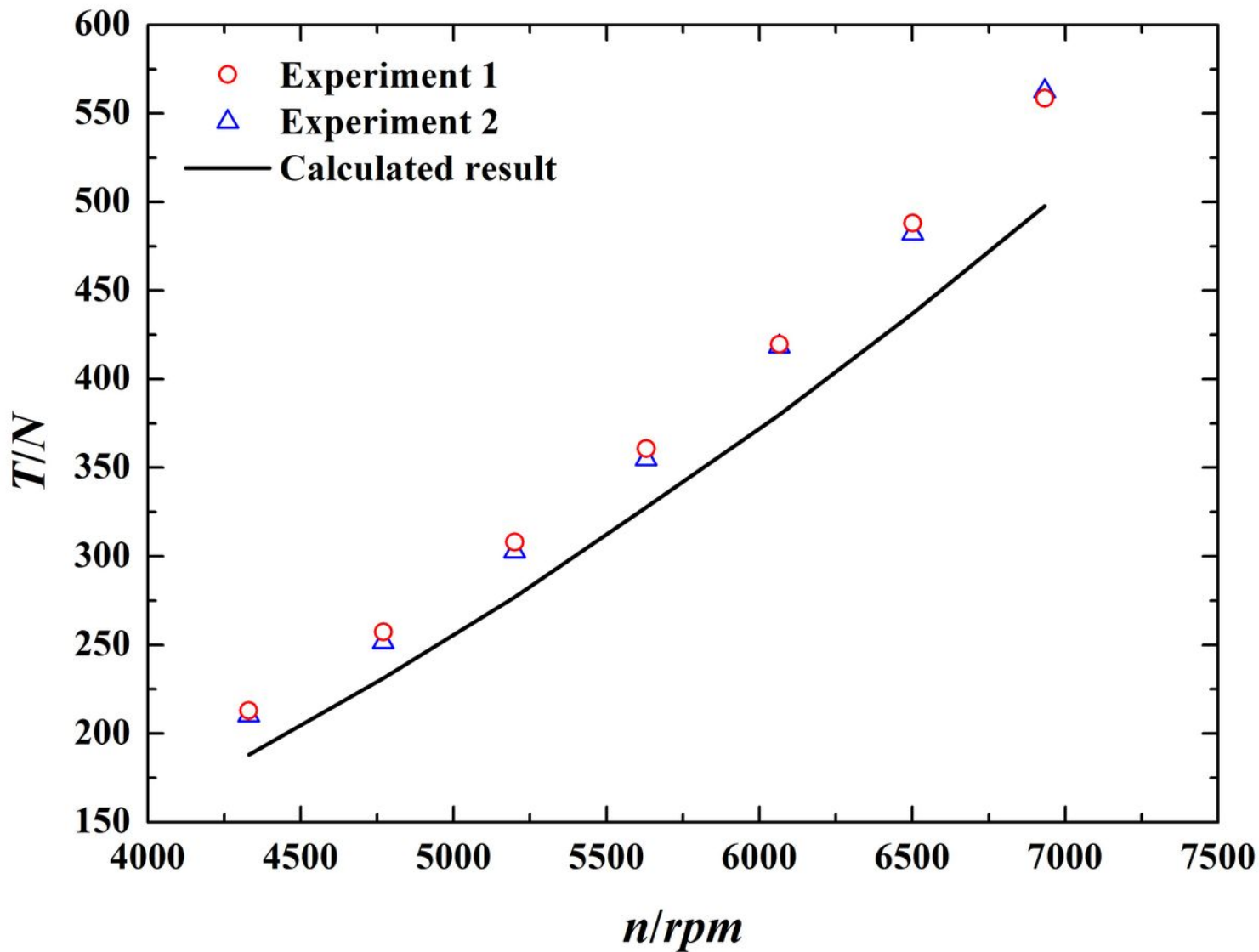


Figure 13

Comparison of axial forces

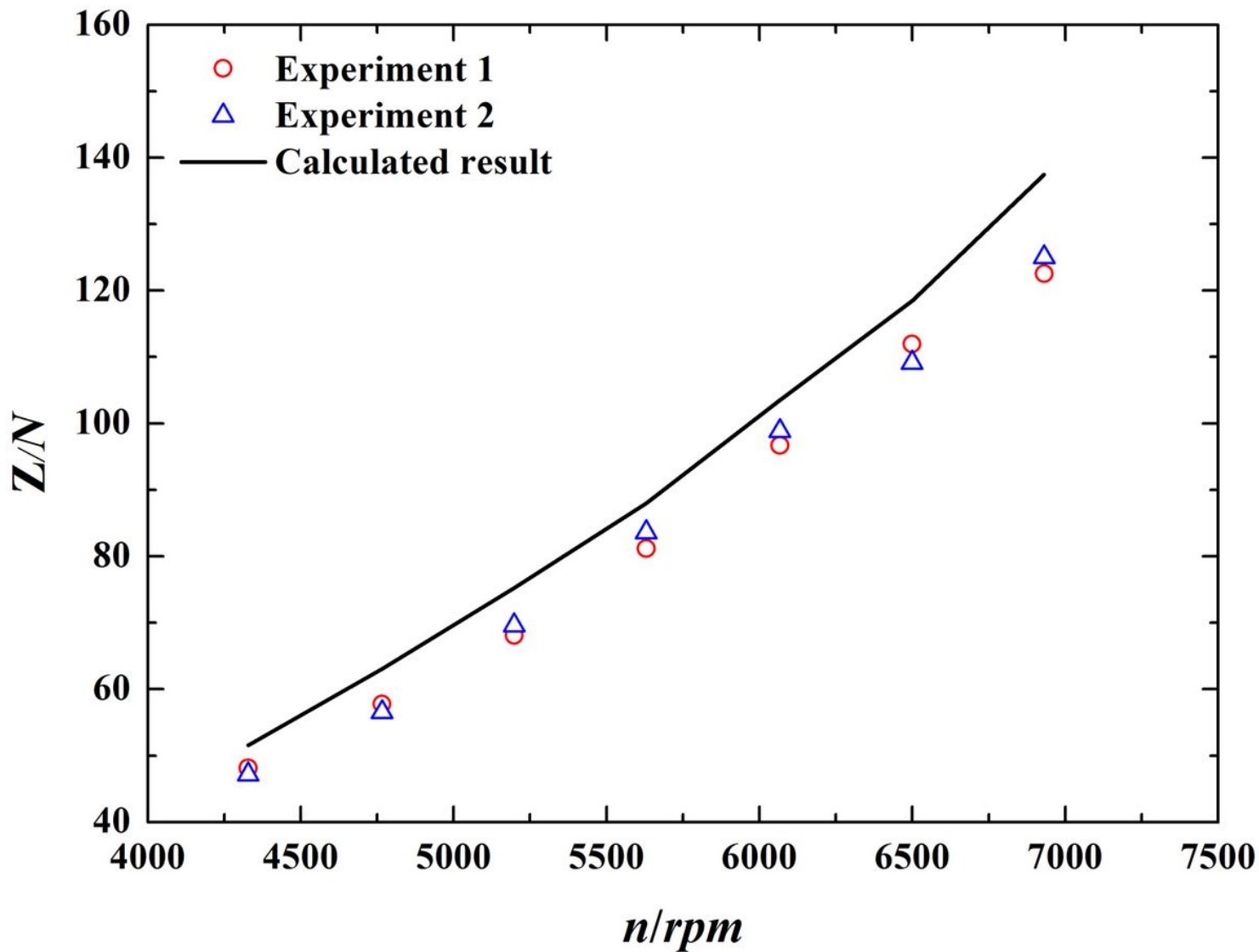


Figure 14

Comparison of lateral force

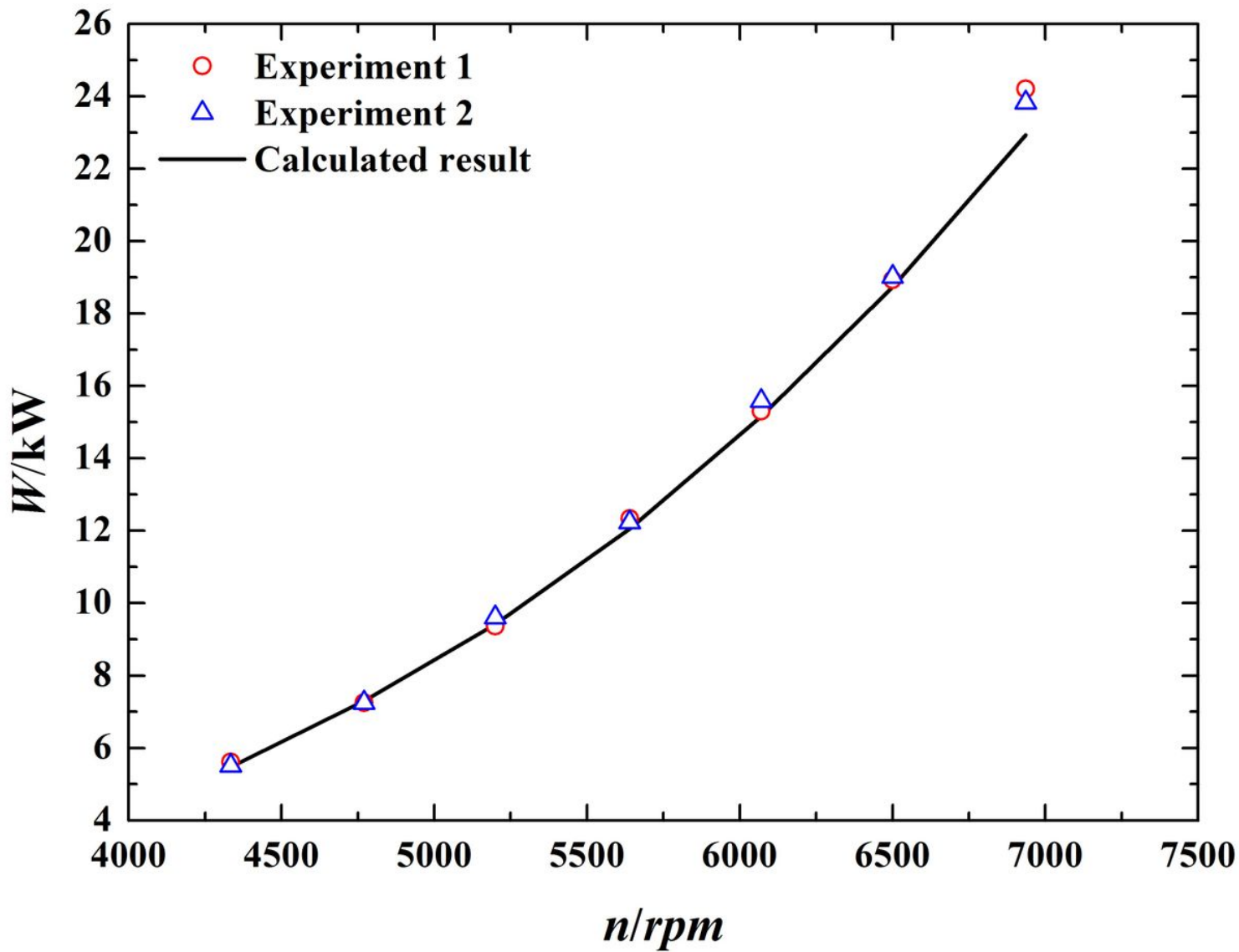


Figure 15

Comparison of power between experiments and calculations

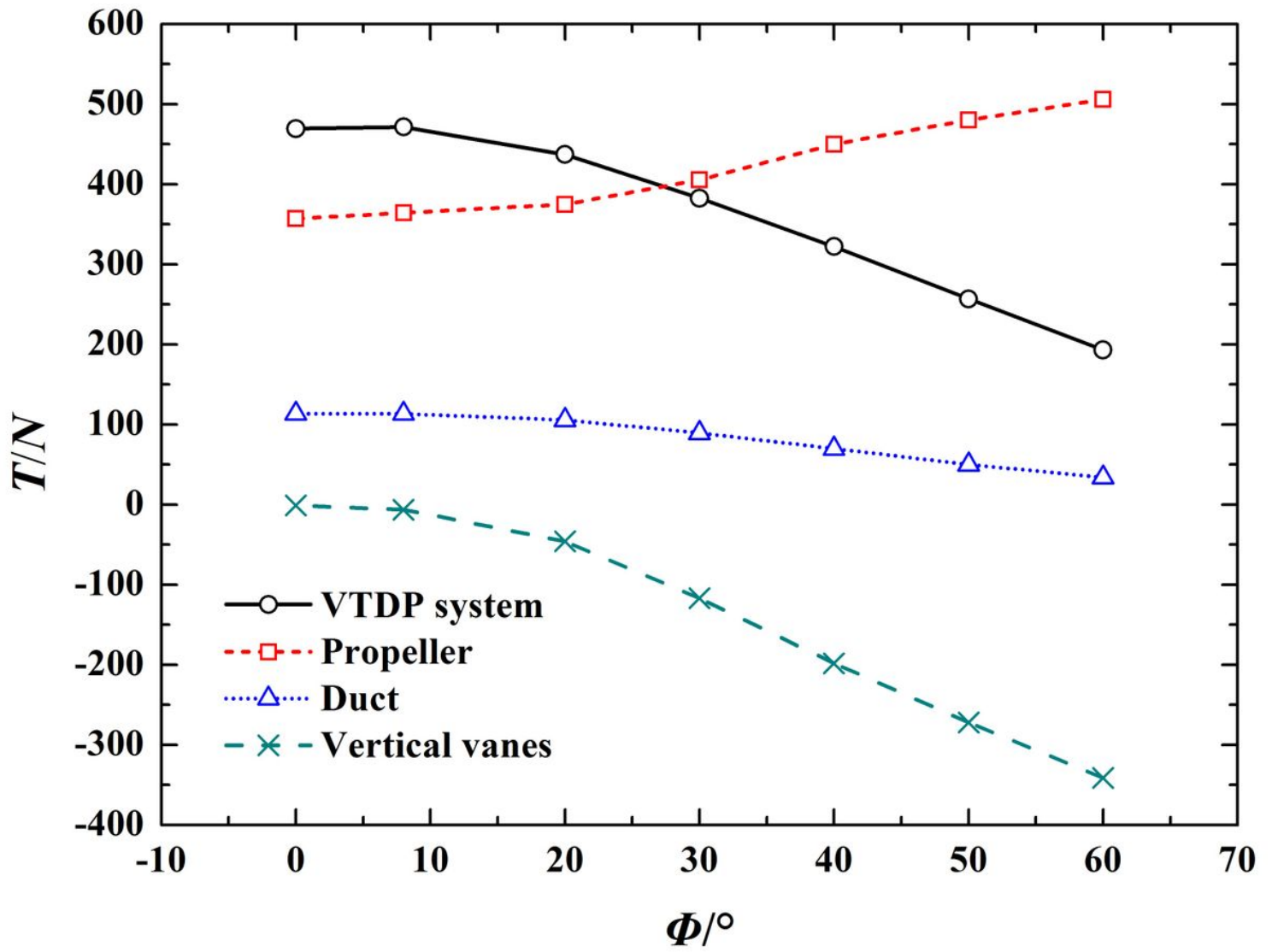


Figure 16

Thrust at different deflection angles

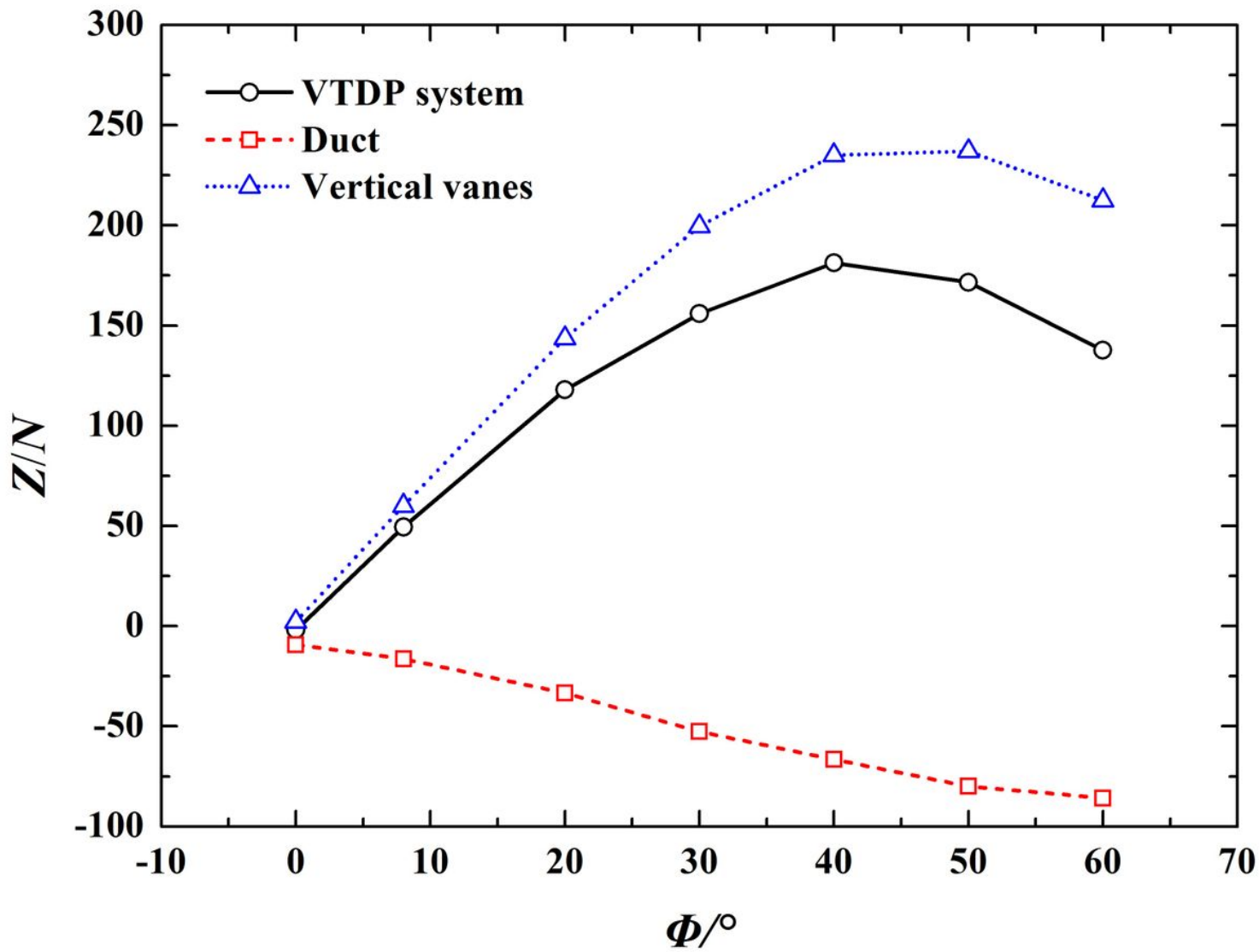


Figure 17

Lateral force at different deflection angles

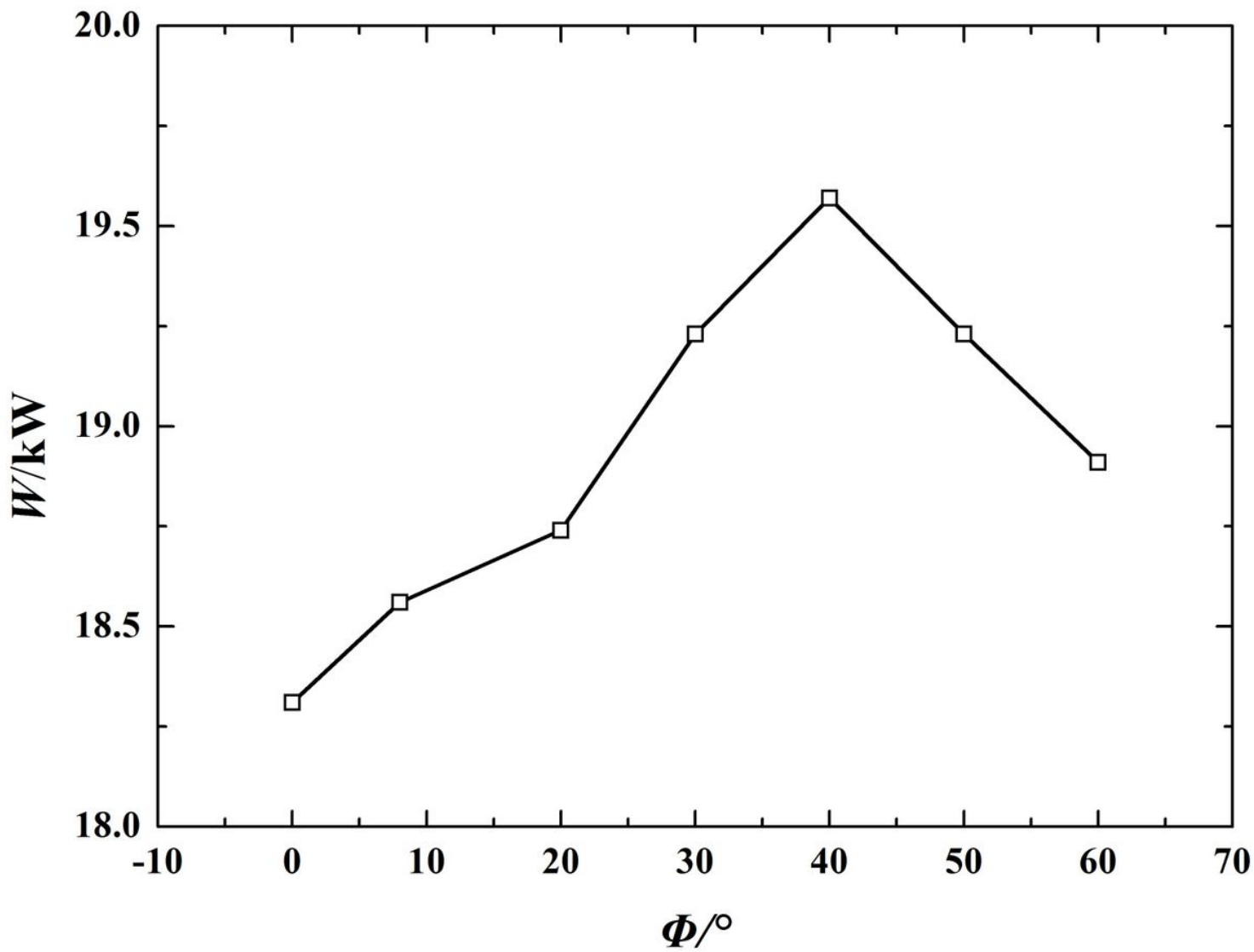


Figure 18

Power at different deflection angles of vanes

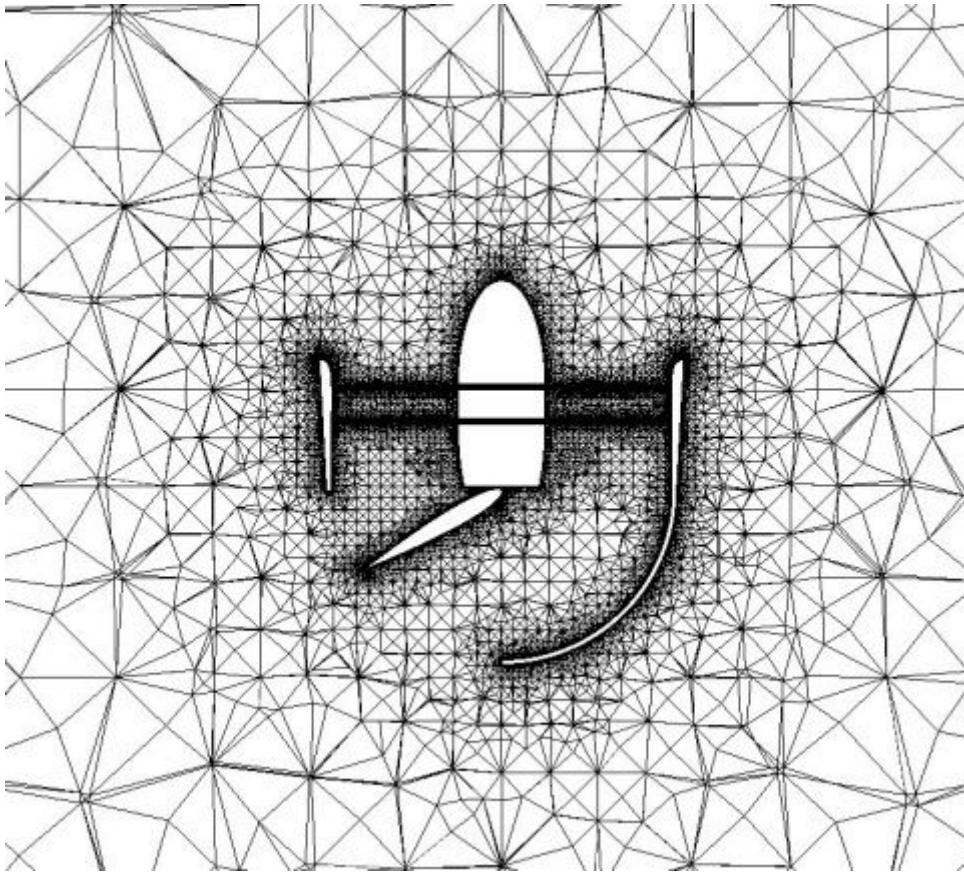
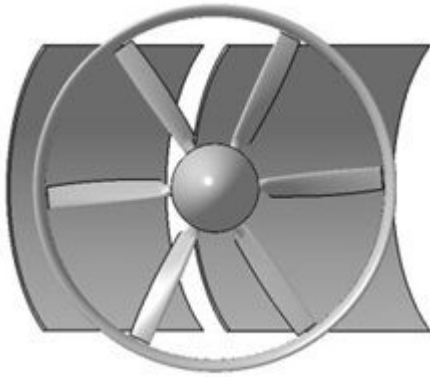
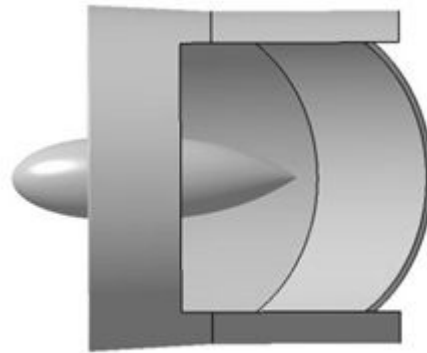


Figure 19

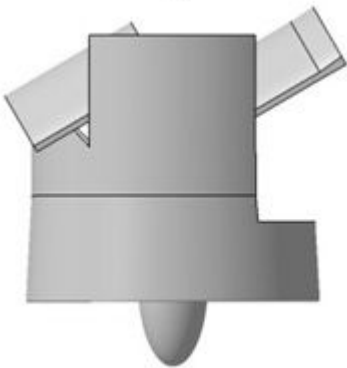
Mesh in the horizontal central section for X-49



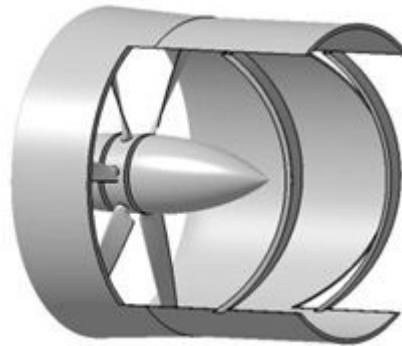
(a)



(b)



(c)



(d)

Figure 20

Conceptual deflection system of VTDP. (a) Front view (b) Right side view (c) Top view (d) 3D view

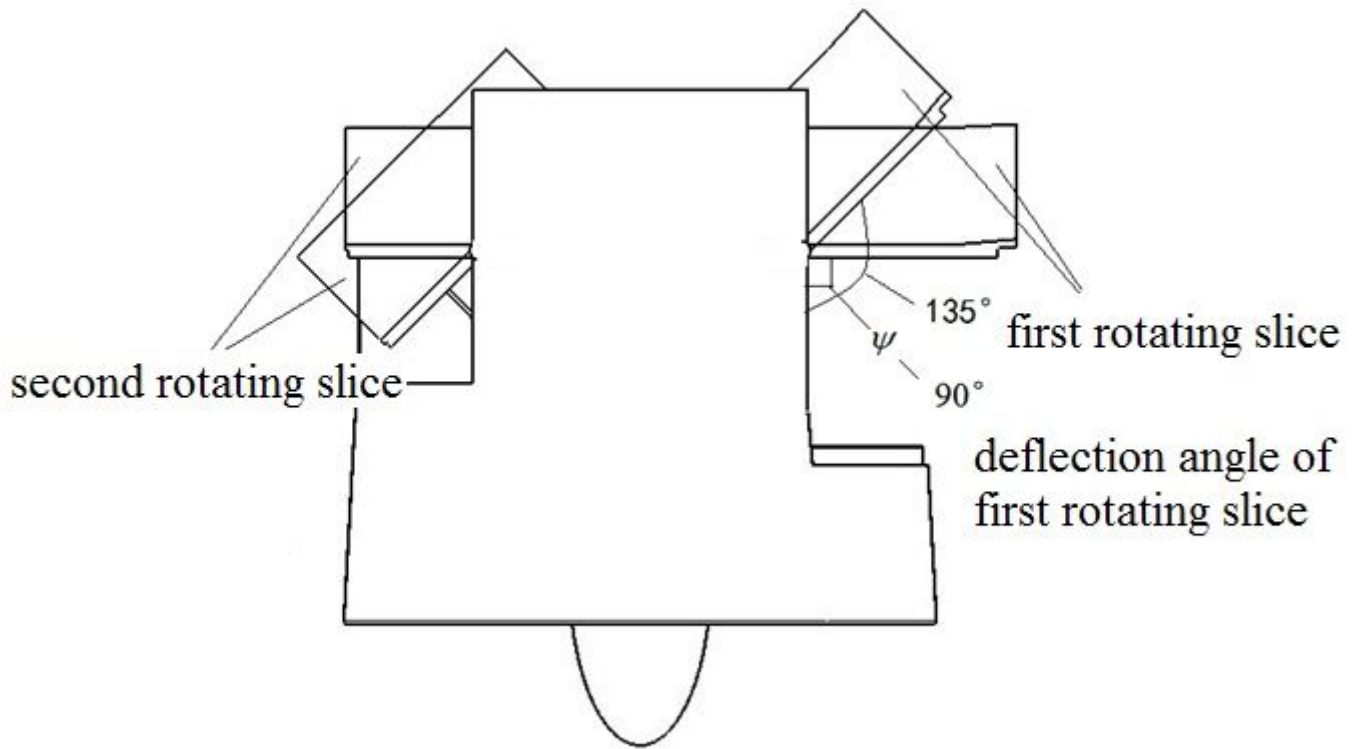


Figure 21

Conceptual deflection system of VTDP at operating conditions

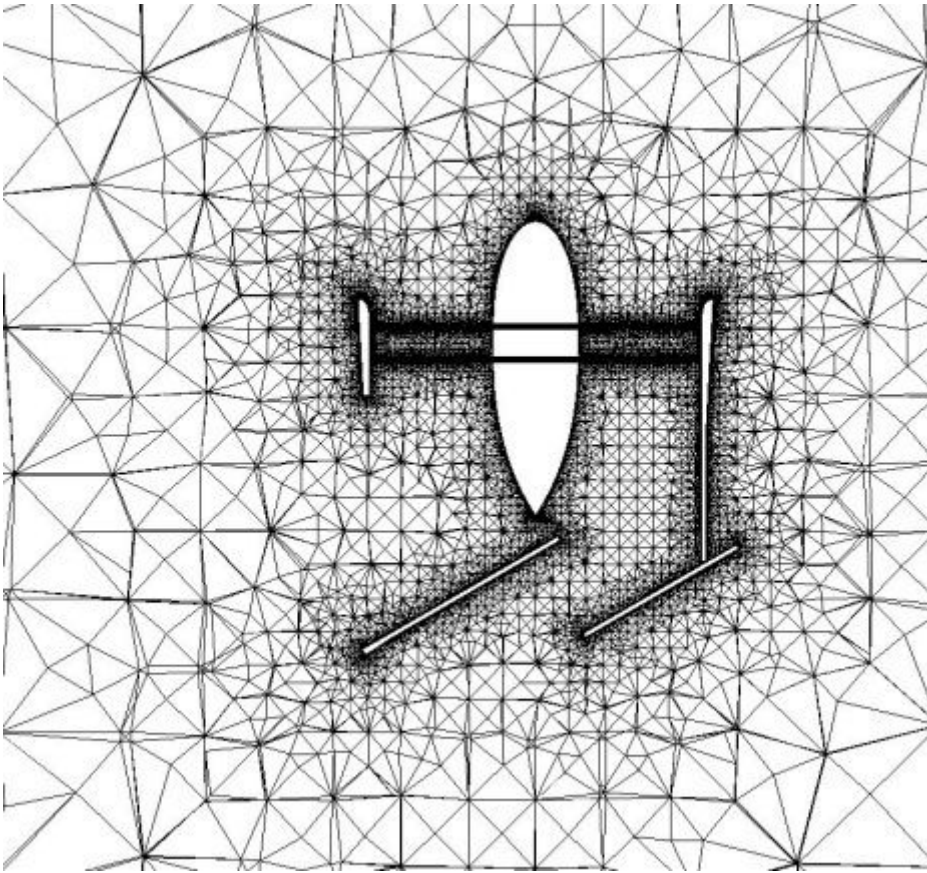


Figure 22

Horizontal central section meshes

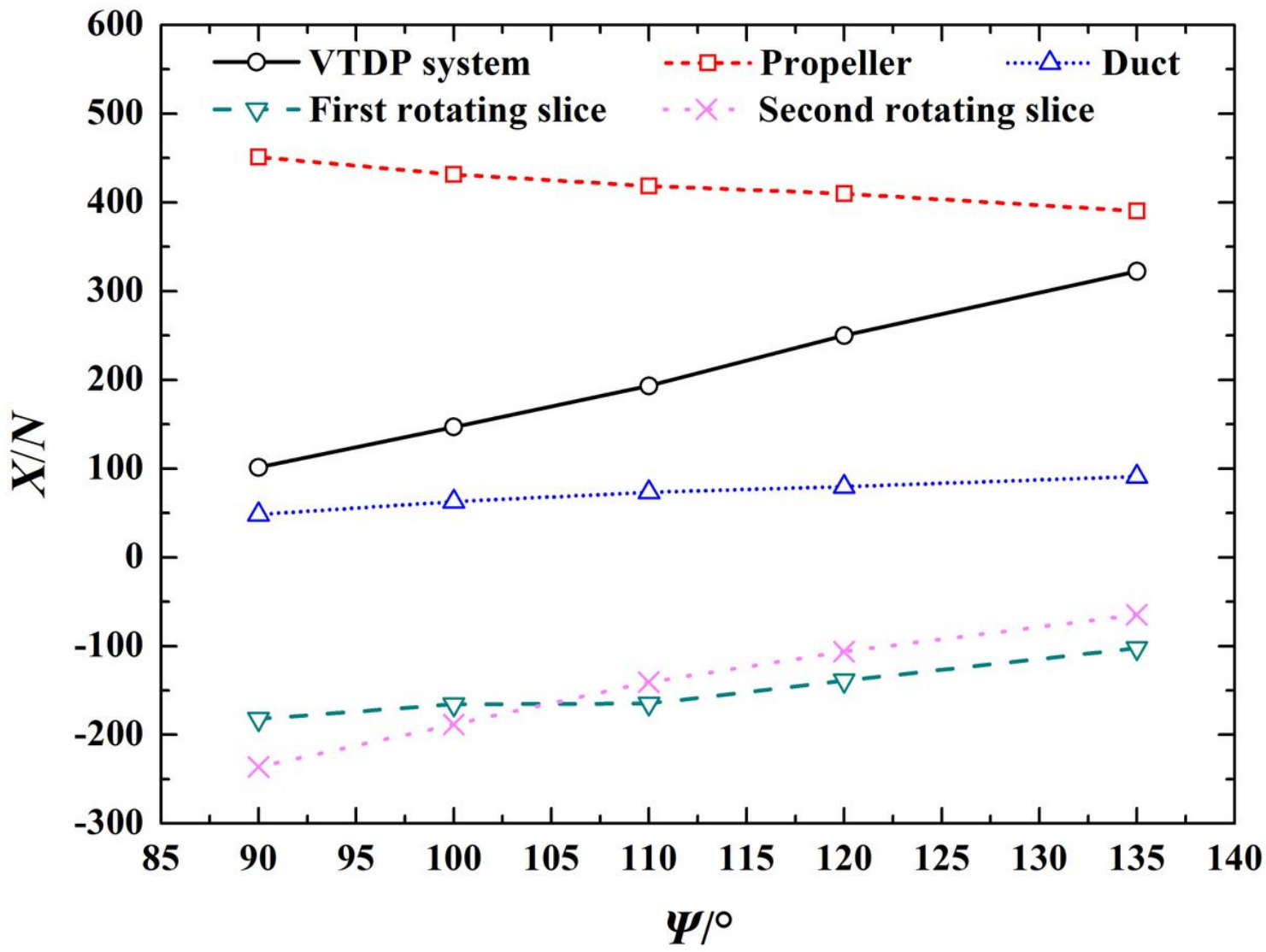


Figure 23

Axial force versus Ψ for conceptual design

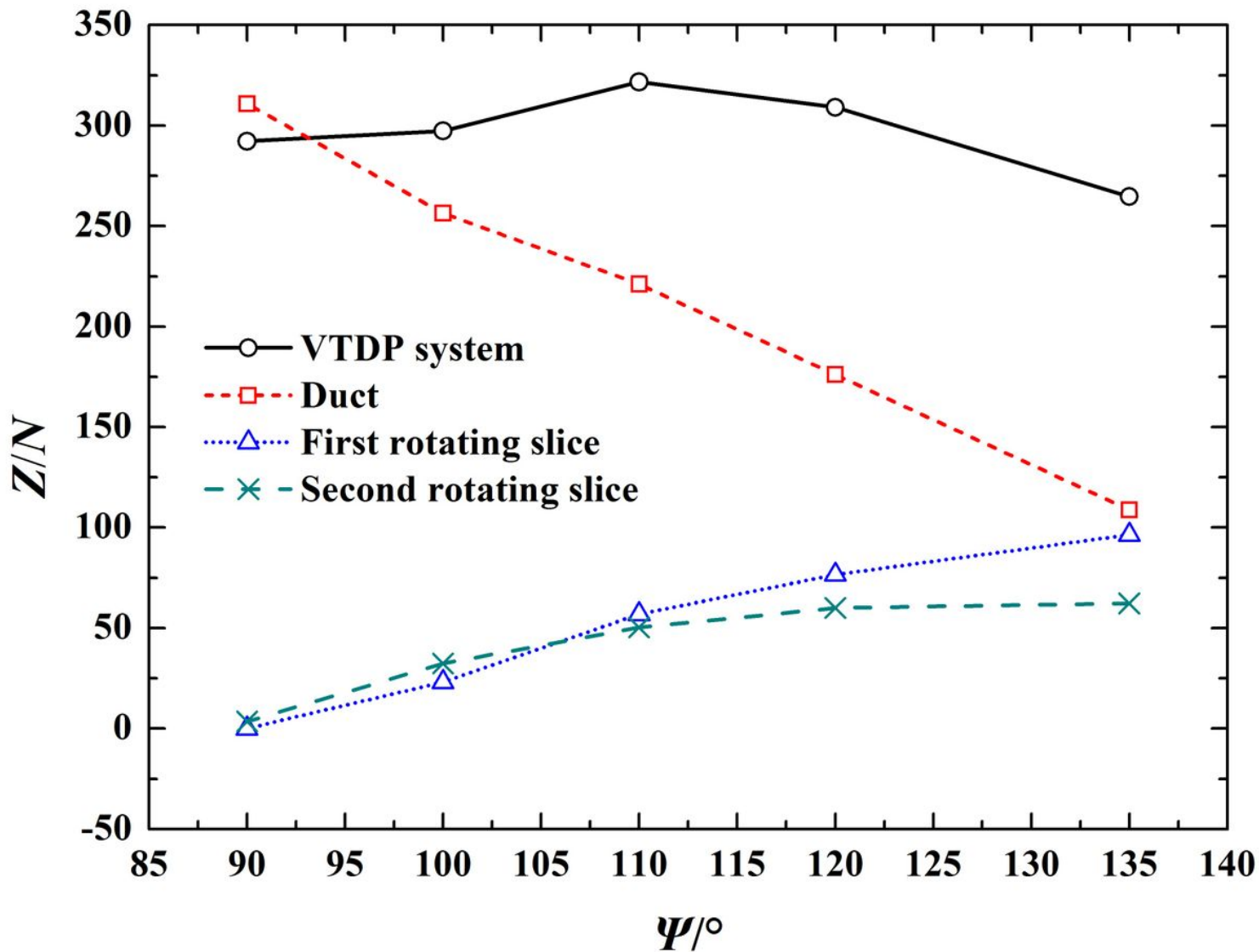


Figure 24

Lateral force versus Ψ for conceptual design

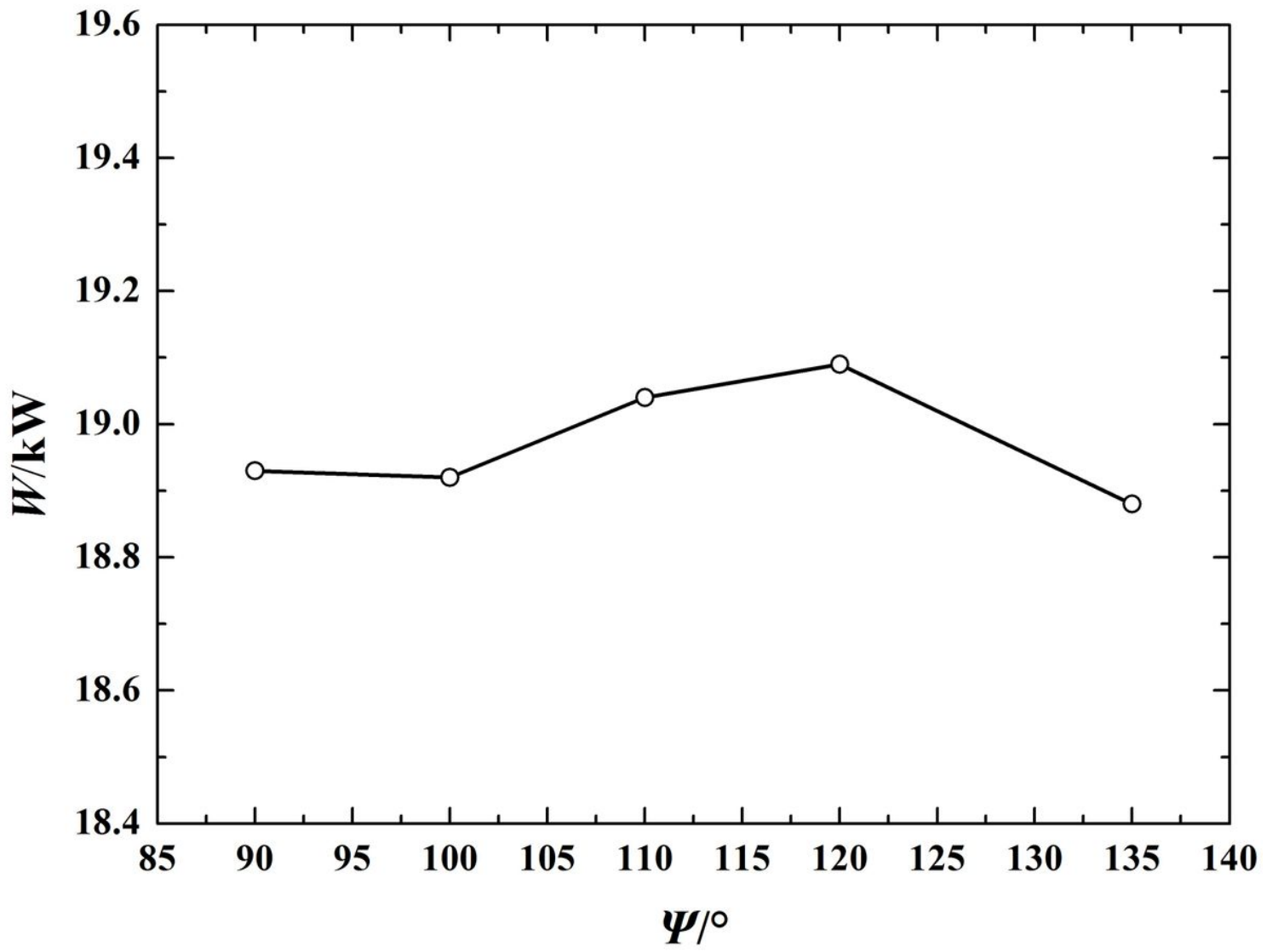


Figure 25

Power versus Ψ for conceptual design

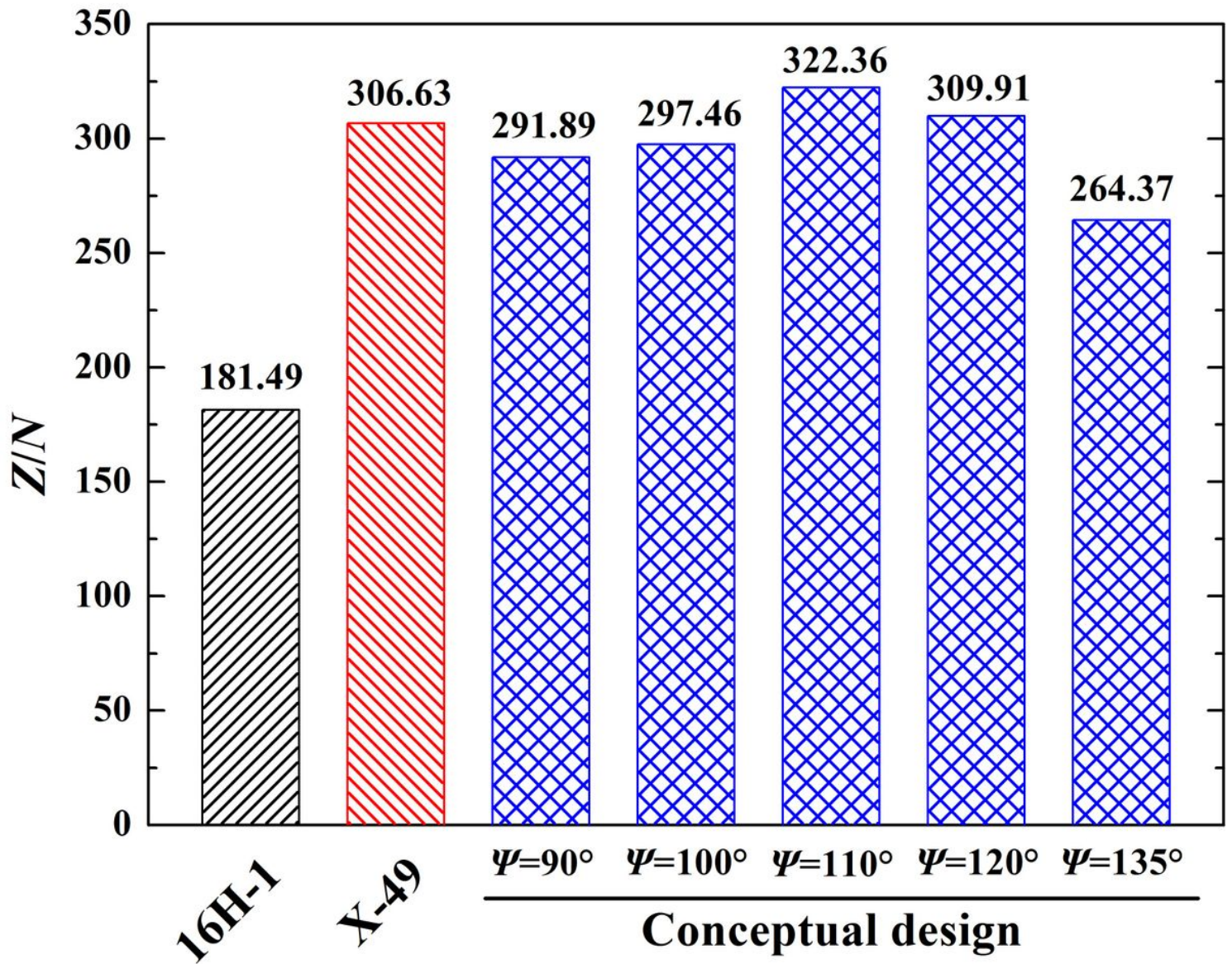


Figure 26

Comparison of lateral forces

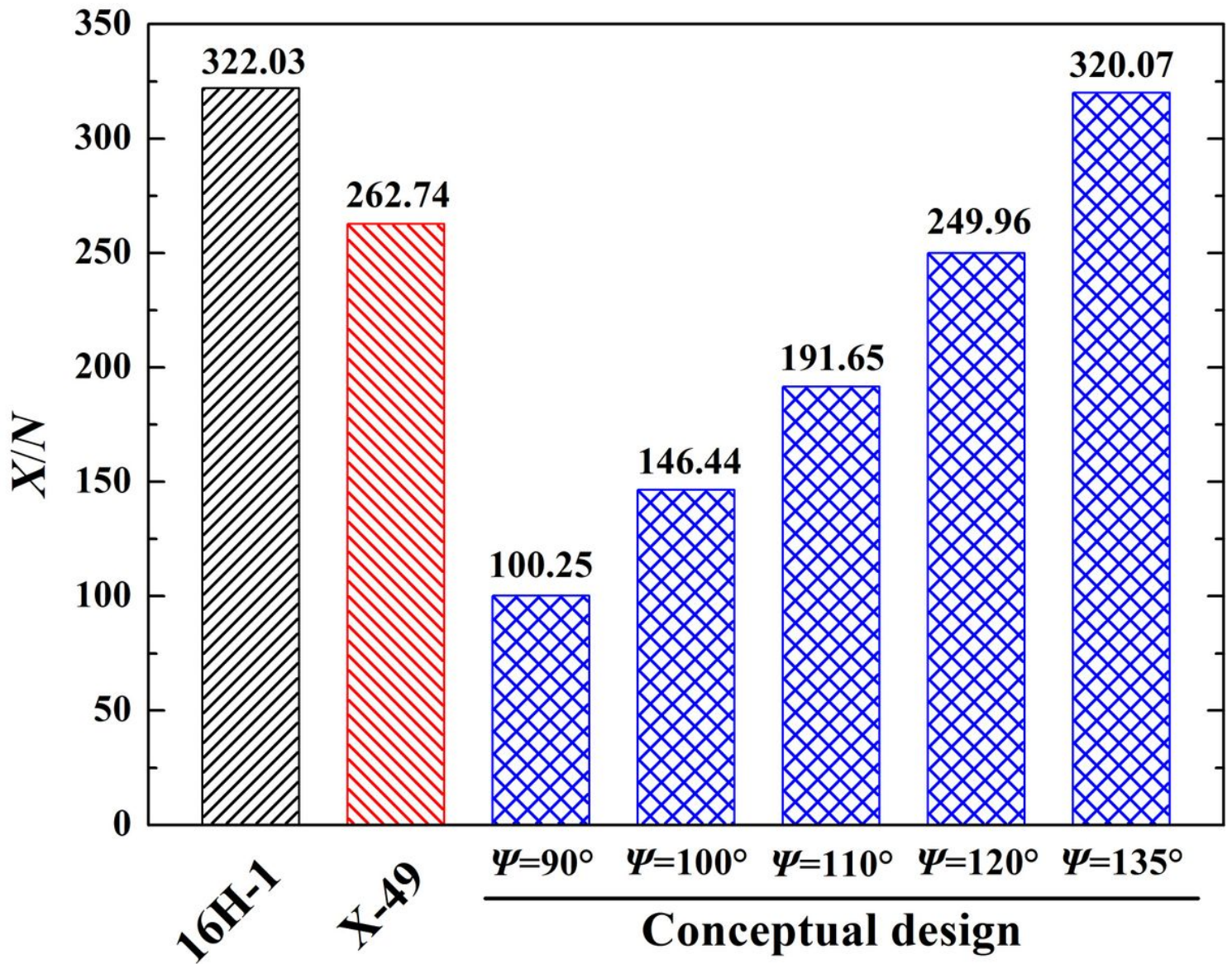


Figure 27

Comparison of axial forces

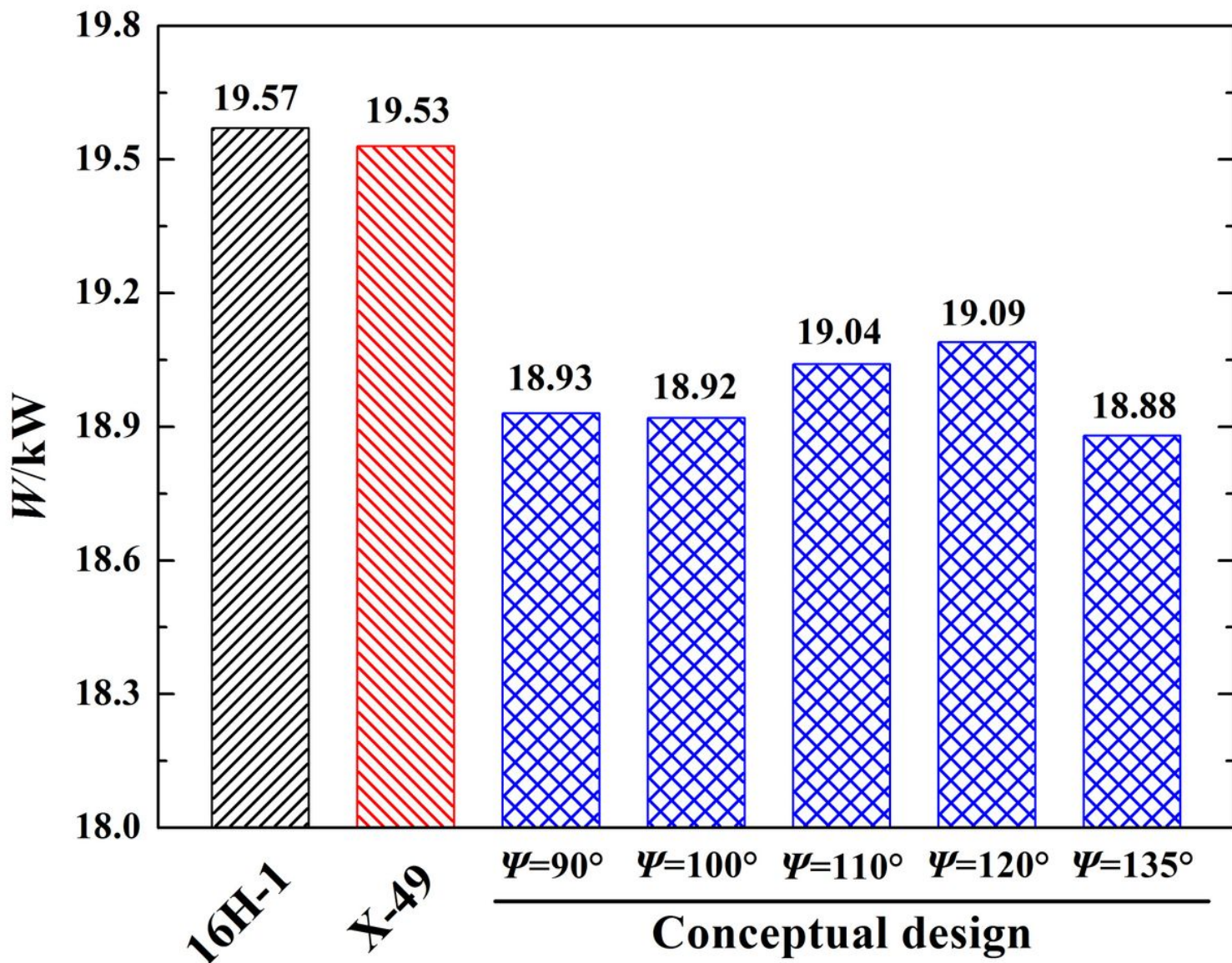


Figure 28

Comparison of power

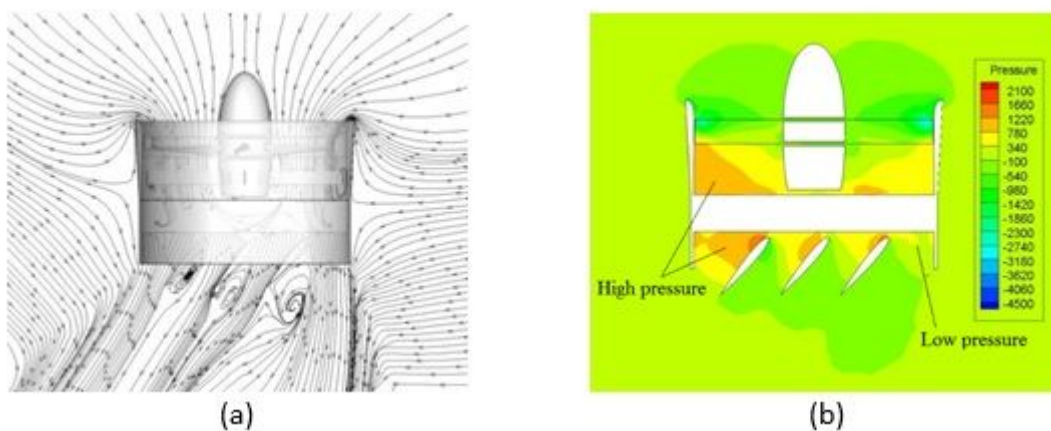


Figure 29

Streamlines and pressure contours for 16H-1 at $\Phi = 40^\circ$. (a) Streamlines (b) Pressure contour

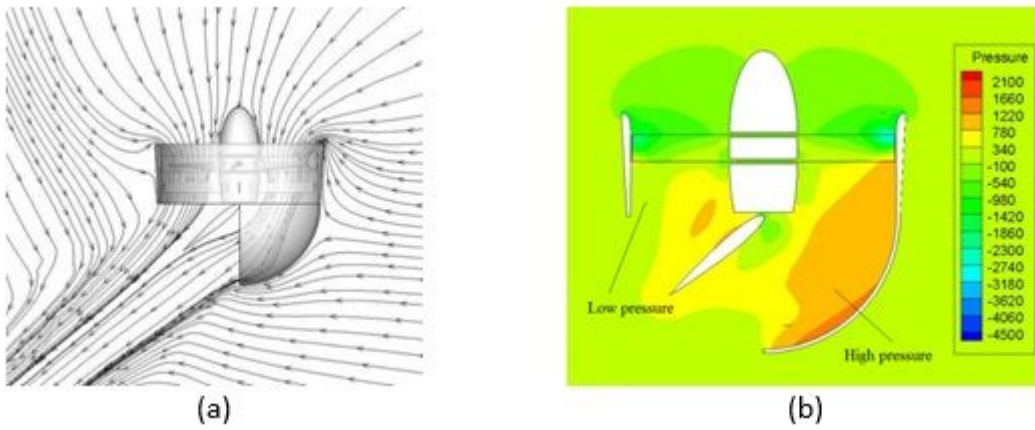


Figure 30

Streamlines and pressure contours for X-49 at $\Phi = 50^\circ$. (a) Streamlines (b) Pressure contour

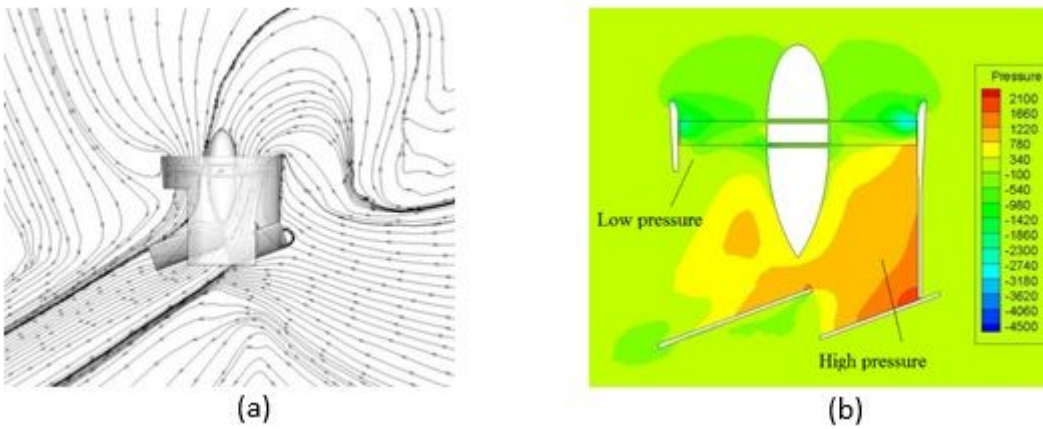


Figure 31

Streamlines and pressure contours for present design at $\Psi = 110^\circ$. (a) Streamlines (b) Pressure contour

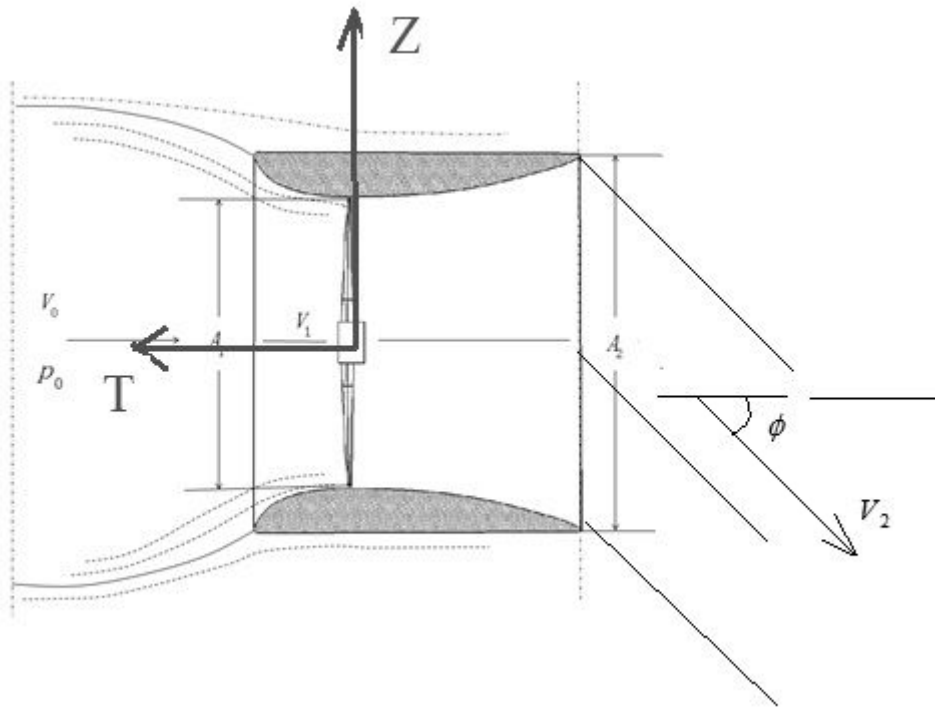


Figure 32

Simplified flow in the VTDP

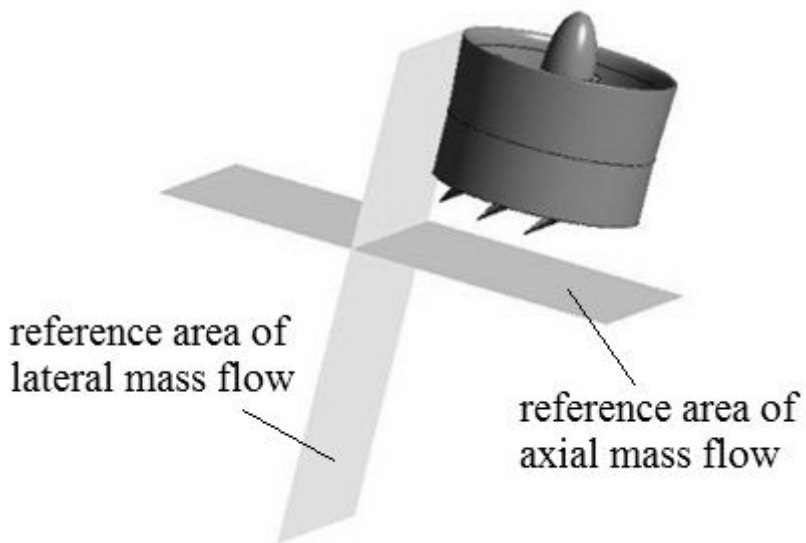


Figure 33

Reference areas for mass flow calculation